Universitetet i Stavanger

FACULTY OF SCIENCE AND TECHNOLOGY

MASTER'S THESIS

Study program/specialisation: Petroleum Engineering/Reservoir technology	Spring semester, 2013 Open
Writer: Finn Arthur Rosland	…… (writers signature)
Faculty supervisor: Steinar Evje	
Title of thesis: Modelling of water-oil flow in reservoirs including effects from gravity, capillary pressure and water rock chemistry	
Credits (ECTS): 30	
Key words: Buckley-Leverett Numerical modelling Low salinity	Pages: …… + enclosure: …… Stavanger, …….. dato/år

Modelling of water-oil flow in porous reservoirs including effects from gravity, capillary pressure and water-rock chemistry

---

Master thesis by Finn Arthur Rosland

Acknowledgments

The subject and writing of this thesis have been motivated by a wish to achieve a more thorough understanding of reservoir modelling and the key physical processes that are involved. In this regard I wish to offer my profound gratitude to my thesis advisor Steinar Evje. From the start your help has been invaluable; first in helping me find an appropriate subject and later with excellent guidance and advice.

Next I would like to show my appreciation to Helmer André Riis and Aruoture Voke Omekeh for their help and advice on low salinity modelling. In that regard I would also like to thank IRIS for use of office space and allowing me to run simulations using the low salinity model.

Special gratitude is offered to my family who have supported me both mentally and physically throughout this process. Without your encouragement and kind words I don't know where I would be today. I especially want to thank my father for his help and support in writing this thesis. Without you to check derivations and bounce ideas off of, I would have been lost.

Last but not least I want to thank my beloved Ane Camilla, and our cherished daughter who was fortunate enough to see first light of day this spring. You have been patient beyond words, and you both mean more to me than can be expressed in words

Abstract

In this work we use mass balance equations to arrive at a classical description of the Buckley-Leverett equation for two phase flow in a one dimensional porous medium.

Through the use of explicit numerical techniques we study the solution of immiscible displacement in an oil-water system. In particular, we study the effect of viscosity, relative permeability, wettability, capillary pressure and gravity. We show that all of these effects are important for oil recovery processes.

These type of models, are very useful when investigating typical reservoir flow behaviour, and when evaluating different enhanced oil recovery (EOR) techniques. In this case, a low salinity model is used to study different 'low salinity' brines in a immiscible displacement process. This model extends the Buckley-Leverett formulation by incorporating a multiple ion exchange (MIE) process. We show that for certain brine compositions, we are able to model positive low salinity effects and thus increase oil recovery.

Table of Contents

1 Introduction

This thesis is focused on studying the behaviour of fluid displacement in a one dimensional two-phase flow model. In particular, the Buckley-Leverett Model is used to investigate frontal advance of water-oil flow in a reservoir model and will be expanded to include effects from water-rock chemical interaction, referred to as the Low Salinity Model. A more detailed description of the structure of this thesis is as follows:

Part 1: This section focuses on basic aspects of the Buckley-Leverett Model. Key subjects are listed below in order of appearance:

- Derivation of the model
- Numerical and analytical solutions
- Model behaviour
- Model expansion including gravity
- Model expansion including capillary pressure

Part 2: In this section, we explore an extended version of the Buckley-Leverett Model where a transport-reaction system is included. The transport-reaction part of the model describes reactions between divalent ions on the rock surface and ion concentrations in low salinity brines injected into a reservoir. The derivation of the model is based on the work by [1], and this model is used to replicate some of the numerical experiments presented in their paper.

All numerical modelling has been performed using MATLAB scripts, and the basis for these scripts has been supplied by the thesis advisor. However, these files have been modified to implement extensions such as normalised water saturation, LET relative permeability, gravity and capillary pressure. Low salinity modelling has been performed using a MATLAB script supplied by the authors of [1], and was run at the International Research Institute of Stavanger.

2 Multiphase flow in porous media

When modelling the behaviour of fluids flowing in porous media, the principle of mass conservation and Darcy's law are used to derive flow equations [2]. These flow equations are a set of differential equations referred to in this text as the mass balance equations (MBE). With the aim to simulate multiphase fluid flow, and hence predict production performance, these equations will be the basis for a variety of different flow models.

In the oil industry, for field development and production purposes, comprehensive three dimensional reservoir models are created in order to run simulations and predict overall performance of hydrocarbon bearing fields; however, it is also useful to use simplified models to investigate certain aspects of the recovery mechanisms/processes involved. One such model was introduced by Buckley and Leverett in 1941, and aims to describe immiscible displacement (water/gas and oil) in sand reservoirs. This model has been widely used in the industry, and expanded to include additional behaviour. In this thesis, the Buckley-Leverett (BL) equation will be derived and discussed in some detail with special focus on expansions including; gravity, capillary pressure and an EOR effect/process referred to as low salinity water injection.

2.1 The mass balance equations

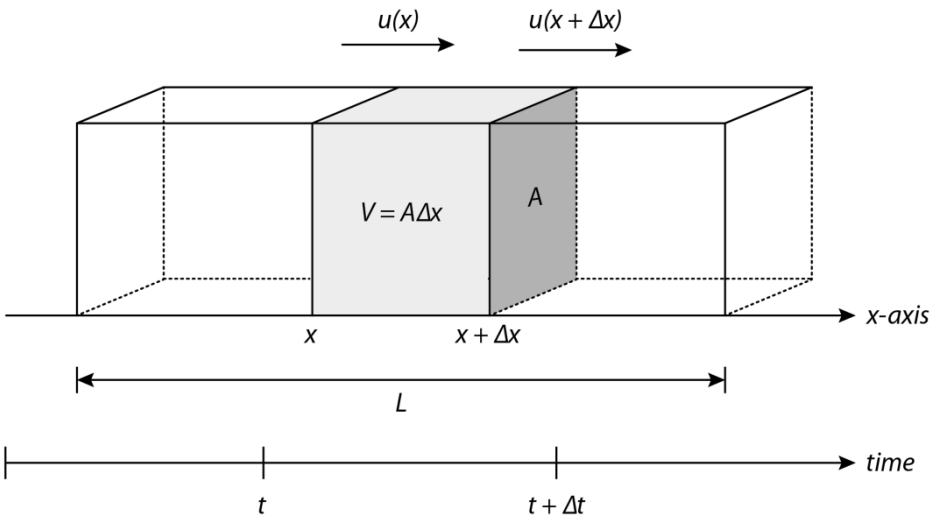

Figure 1: Figure illustrating key aspects of the principles of conservation of mass, used to derive mass balance equations for a 1D reservoir. Based on a figure from [2].

Consider the one dimensional reservoir illustrated in Figure 1, where the reservoir has constant cross-sectional area A and length L. Now assume that one fluid is flowing through this porous reservoir with fluid density ρ and rock porosity φ. Using the principles of mass conservation and Darcy fluid velocity u it is possible to derive the differential equation

$$\frac{\partial}{\partial t}(\varphi\rho) + \frac{\partial}{\partial x}(u\rho) = 0 \tag{2.1}$$

referred to as the mass balance equation for one dimensional single phase flow, also called the diffusivity equation.

Darcy's law describes the principals of fluid flow through porous media, and gives a relationship between fluid velocity and pressure drop across a reservoir. Introducing a proportionality coefficient, k (permeability), the expression for this relationship becomes

$$q = -\mathrm{A}\frac{k}{\mu}(\Delta p + \rho g \Delta z) \tag{2.2}$$

where q represents fluid flow rate, A the cross-sectional area, μ is viscosity, Δp is the phase pressure difference, ρ is fluid density, g is the gravitational constant and Δz is the height of the fluid in direction of the gravitational field.

In terms of superficial velocity (or Darcy velocity), equation (2.2) can be rewritten as

$$u = \frac{q}{A} = -\frac{k}{\mu}(\Delta p + \rho g \Delta z) \tag{2.3}$$

Substituting Darcy velocity into equation (2.1) gives a mass balance equation of the form

$$\frac{\partial}{\partial t}(\varphi\rho) - \frac{\partial}{\partial x}\left[\frac{k\rho}{\mu}\left(\frac{\partial p}{\partial x} + \rho g \Delta z\right)\right] = 0 \tag{2.4}$$

Similarly the mass balance equation including other complexities such as multiple phases, heterogeneities and multiple dimensions can be derived. However, the focus of this paper will be on one dimensional reservoirs with two flowing phases.

2.2 The Buckley-Leverett equation

Water flooding is an immiscible displacement process, almost synonymous with the term secondary recovery, and thus an essential process field of reservoir engineering. As Buckley and Leverett [3] discuss, the natural displacement energy present in a crude oil is very small (i.e. in primary oil recovery processes). To deplete the reservoir efficiently other processes, such as natural or supplementary water displacement, are needed. In their paper Buckley and Leverett introduce a simplified MBE where they use fractional flow and water saturation to model frontal advance in a reservoir.

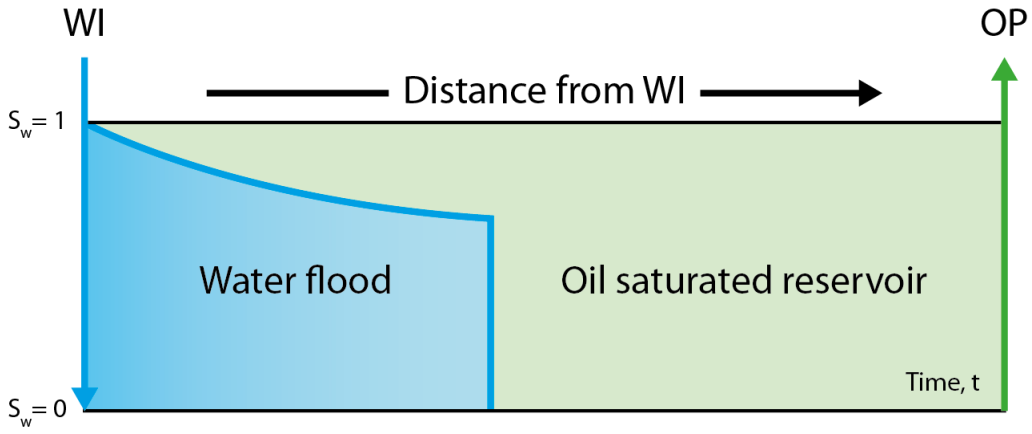

Figure 2: Simplified reservoir model illustrating frontal advance (Buckley-Leverett theory) in a porous medium.

To derive the BL equation we will assume two phase flow through a horizontal 1D reservoir, with constant cross-sectional area and constant length. Furthermore we will assume that the fluids (oil and water) are incompressible and flow through a homogeneous and incompressible reservoir rock. Initially effects due to capillary pressure are also ignored.

The initial conditions state that the reservoir will be oil filled and the boundary conditions consist of water being injected at one end and oil produced at the other end. We will assume that injection and production rates remain constant and that a unique solution does exist.

Based on these assumptions it can be shown, in the same ways as for equation (2.4), that the MBE for oil and water phases can take the form

$$\varphi \frac{\partial S_l}{\partial t} - \frac{\partial}{\partial x}\left(\frac{k k_{rl}}{\mu_l}\frac{\partial p}{\partial x}\right) = 0, \qquad l = o, w \tag{2.5}$$

where k is absolute permeability, k_{rl} is phase relative permeability and S_l is phase saturation. Note also that subscript o and w indicate oil and water respectively. Based on our assumptions, k, μ_l and φ are constants, while k_{rl} has no explicit spatial dependence.

Introducing phase mobilities

$$\lambda_l = \frac{k k_{rl}}{\mu_l}, \qquad l = o, w \tag{2.6}$$

equation (2.5) can be rewritten

$$\varphi \frac{\partial S_l}{\partial t} - \frac{\partial}{\partial x}\left(\lambda_l \frac{\partial p}{\partial x}\right) = 0, \qquad l = o, w \tag{2.7}$$

Adding the water and oil equation, and considering the saturation constraint

$$S_w + S_o = 1 \tag{2.8}$$

we get

$$\frac{\partial}{\partial x}\left(\lambda_t \frac{\partial p}{\partial x}\right) = 0, \qquad \lambda_t = \lambda_w + \lambda_o \tag{2.9}$$

The total flux (total Darcy velocity) is given by

$$u = -\lambda_t \frac{\partial p}{\partial x} \tag{2.10}$$

and therefore u has no special dependence. Now, defining fluid fluxes (phase velocities) as

$$u_l = -\lambda_l \frac{\partial p}{\partial x}, \qquad l = o, w \tag{2.11}$$

and the total flux as $u = u_w + u_o$, it follows that

$$\frac{\partial p}{\partial x} = -\frac{u}{\lambda_t} \tag{2.12}$$

Eliminating the pressure equation in the MBE for the water phase will then give

$$\varphi \frac{\partial S_w}{\partial t} + u \frac{\partial}{\partial x}\left(\frac{\lambda_w}{\lambda_t}\right) = 0 \tag{2.13}$$

Since the system is assumed to be horizontal, with gravity and capillary forces negligible we can express fractional flow in the form [4]

$$f_w = \frac{\frac{kk_{rw}}{\mu_w}}{\frac{kk_{ro}}{\mu_o} + \frac{kk_{rw}}{\mu_w}} = \frac{\lambda_w}{\lambda_t} \tag{2.14}$$

where $f_w = f_w(S_w)$ and this results in the MBE

$$\varphi \frac{\partial S_w}{\partial t} + u \frac{\partial f_w}{\partial x} = 0, \tag{2.15}$$

commonly referred to as the BL equation.

2.2.1 Dimensionless form

Using dimensionless variables we can express the BL equation in a more convenient form. We introduce the dimensionless special variable x_D, using the total length of the reservoir, L

$$x_D = \frac{x}{L} \Rightarrow \frac{\partial f_w}{\partial x_D}\frac{\partial x_D}{\partial x} = \frac{\partial f_w}{\partial x_D}\frac{1}{L} \tag{2.16}$$

Similarly we introduce a dimensionless time variable, t_D, using the total volumetric rate q and the pore volume $A\varphi L$:

$$t_D = \frac{qt}{A\varphi L} \Rightarrow \frac{\partial S_w}{\partial t_D}\frac{\partial t_D}{\partial t} = \frac{\partial S_w}{\partial t_D}\frac{u}{\varphi L} \tag{2.17}$$

Note that the dimensionless time variable, t_D, will also represent the fraction of injected pore volume (PV).

It is now convenient to substitute t for t_D, x for x_D, S for S_w and f for f_w. Using the new dimensionless variables and new notation, the BL equation has the form

$$\frac{\partial S}{\partial t} + \frac{\partial f}{\partial x} = 0 \tag{2.18}$$

In addition, we need boundary conditions at $x = 0$ for $t \geq 0$, and the initial conditions for $0 \leq x \leq 1$ at $t = 0$.

An example of the frontal advance solution of (2.18) is shown in Figure 3 for three different time values; 0.1, 0.2 and 0.4. An initial condition of 100% oil saturation was used, and a boundary condition of 100% water saturation at $x = 0$.

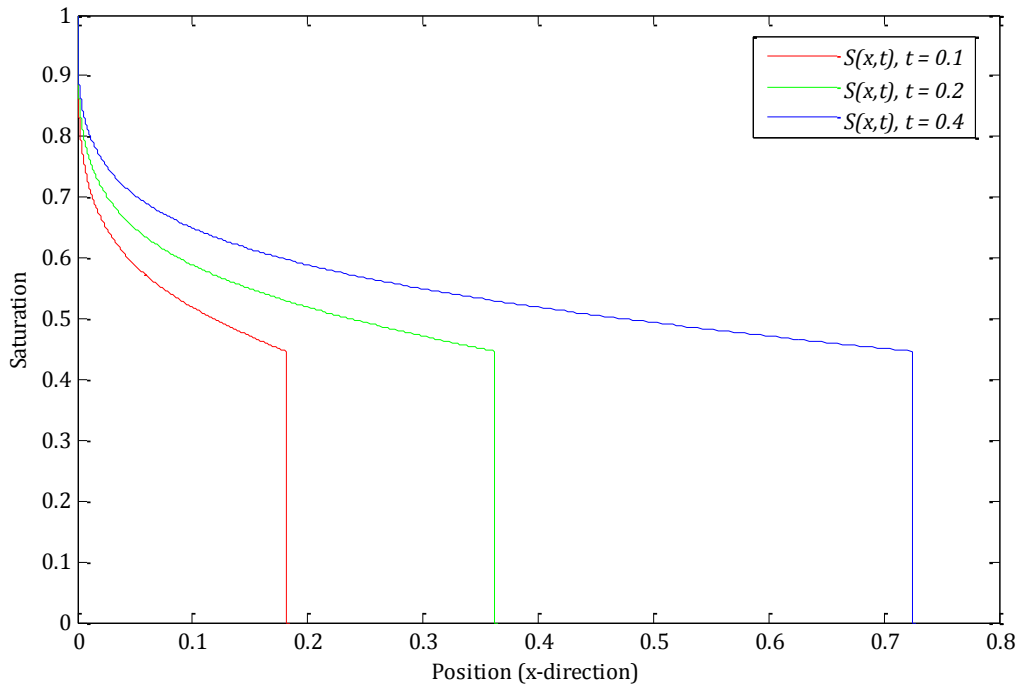

Figure 3: Plot showing frontal advance at three dimensionless time values, t=0.1, t=0.2 and t=0.4. See Appendix A for other input parameters.

2.3 Solution procedures

Specific types of differential equations, such as the BL equation, can be solved analytically though it is often more practical to use numerical techniques; but in cases where an analytical solution does not exist, one has to resort to numerical solution methods. In this thesis the main focus will be on the numerical solutions.

2.3.1 Analytical solution

In equation (2.18) f is a function of the saturation S only, and therefore has no explicit x dependence, and the expression can be written as

$$\frac{\partial S}{\partial t} + f'(S)\frac{\partial S}{\partial x} = 0 \tag{2.19}$$

Assume that there exists a unique solution for $S = S(x,t)$ of the equation (2.19); and consider a set of points in the x-t plane which define a smooth curve $g = [x(t), t]$. Let the saturation along these curves be described by the function $h(t) = S(x(t), t)$, which is only dependent on the single variable t. If we now differentiate h with respect to t, we get the expression

$$\frac{dh}{dt} = \frac{\partial S}{\partial t} + \frac{\partial S}{\partial x}\frac{dx}{dt}. \tag{2.20}$$

If the curves have been chosen such that g satisfies the condition

$$\frac{dx}{dt} = f'(S), \tag{2.21}$$

it follows from (2.19), (2.20) and (2.21) that

$$\frac{dh}{dt} = \frac{\partial S}{\partial t} + f'(S)\frac{\partial S}{\partial x} = 0 \tag{2.22}$$

This equation tells us that the saturation is constant along these curves. It also implies that $f(S)$ and $f'(S)$ are constant along the same curves. From (2.21) we therefore note that the smooth curves g in the x-t plane are straight lines. Note that the physical implication of these observations is that every point on the saturation curve will have a constant velocity $f'(S)$.

The solutions for equation (2.21) can be written as

$$x(t) = x_0 + f'(S_0)t \tag{2.23}$$

where a and S_0 are constant. By varying x_0 and S_0 we will get a family of g curves along which the saturation is constant.

Using initial conditions $S(x,0) = 0$ and the boundary condition $S(0,t) = 1$, the equation (2.23) can be rewritten as

$$x(t) = f'(S_0)t \tag{2.24}$$

The family of g curves in this case is shown in Figure 4.

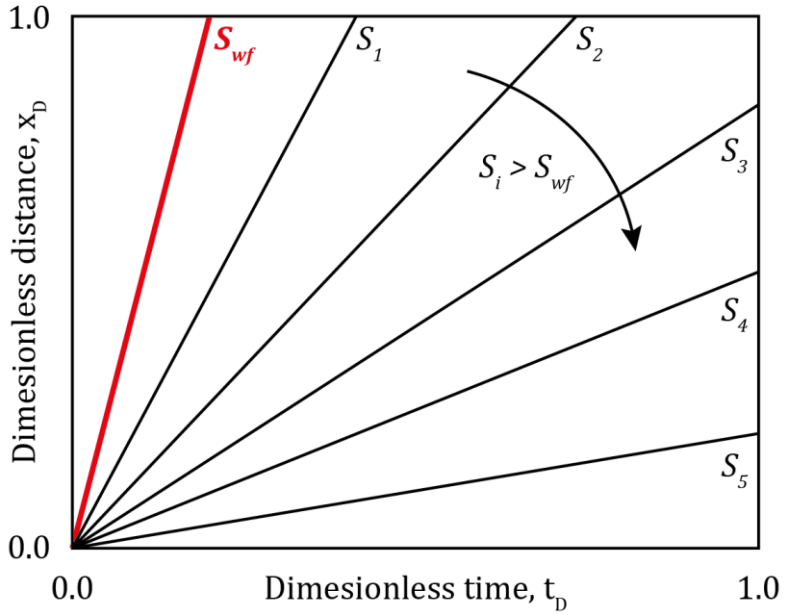

Figure 4: Schematic illustration showing a set of g curves as straight lines in the x_D-t_D plane. Each curve represents a constant saturation value, and the slope of these lines gives the velocity, $f'(S)$, of that point on the saturation curve.

However, the frontal advance solution will have a non-physical solution since there are two saturation values for every position value, x, at an elapsed time, T (see Figure 5). The physical solution will instead have a shock front, with flood front saturation, S_f, and across the front this saturation will fall to the initial water saturation value (zero in our case). The position of the front can be determined analytically by using a material balance equation. This is done by comparing the integral of the two frontal advance solutions:

$$\int_0^1 f'(S)TdS = \int_{S_f}^1 f'(S)TdS + f'(S_f)TS_f = T \tag{2.25}$$

and from this we obtain the linear relation $f'(S_f)S_f = f(S_f)$, from which S_f is determined.

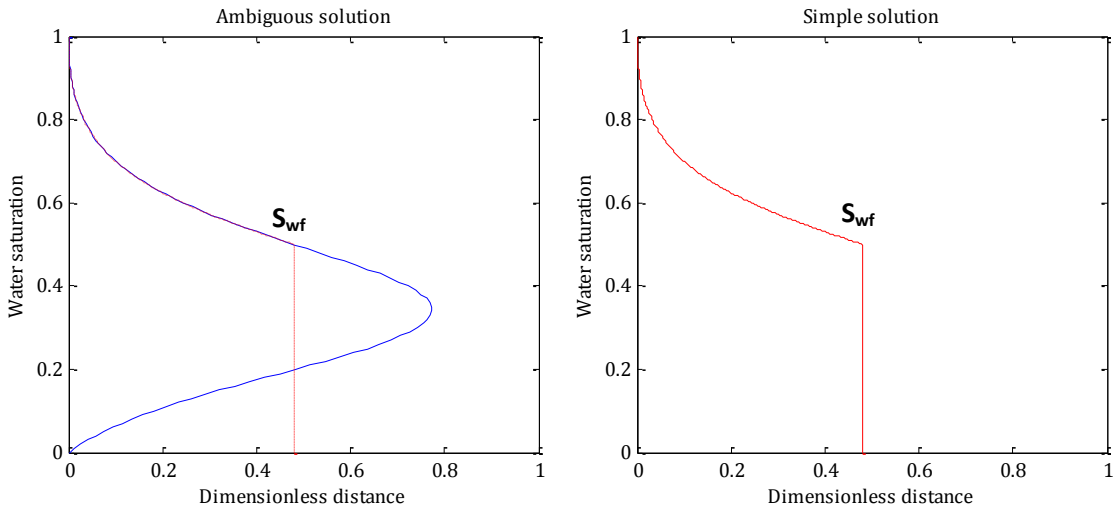

Figure 5: Plots showing a comparison between the ambiguous (non-physical) and simple (shock front) solutions using the analytical solution procedure for the Buckley-Leverett Model. Elapsed time is the same in both cases. Left: ambiguous solution. Right: simple solution. See Appendix A for other input parameters.

2.3.2 Numerical solution

The first step in a numerical solution of a partial differential equation will consist of discretizing the equation for all variables. This procedure leads to a set of algebraic equations.

A consequence of the discretization procedure is the introduction of computational error. In general this error will effect the numerical stability of the solution. Numerical stability can be defined as:

> *a difference scheme is stable if a computational error introduced at one time step does not grow at computations for subsequent time steps* [2].

There are a number of different schemes that can be used, but to illustrate the numerical solution procedure used in this thesis, an explicit scheme has been applied. Using a shorthand notation we can express equation (2.18) in the form

$$\partial_t S + \partial_x f(S) = 0 \tag{2.26}$$

Discretizing this equation gives the expression

$$\frac{1}{\Delta t}\left(S_j^{n+1} - S_j^n\right) + \frac{1}{\Delta x}\left(f_{j+\frac{1}{2}}^n - f_{j-\frac{1}{2}}^n\right) = 0 \tag{2.27}$$

where the time index is $n \geq 1$ while j is the spatial index with $1 \leq j \leq N_x$. In this case Δt and Δx are the temporal and spatial cell size increments, and are assumed constant.

We can now solve equation (2.27) for the saturation at time-step $n+1$ and get

$$S_j^{n+1} = S_j^n - \frac{\Delta t}{\Delta x}\left(f_{j+\frac{1}{2}}^n - f_{j-\frac{1}{2}}^n\right) \tag{2.28}$$

Note that in this thesis the numerical experiments have been designed using a more complex MUSCL schema with the van Leer limiter, where the definition of $f_{j+\frac{1}{2}}^n$ and $f_{j-\frac{1}{2}}^n$ are described. Details about this difference scheme is more complex and outside the scope of this thesis.

It can be shown that the stability of the numerical solution depends on the term $\Delta t/\Delta x$. Typically numerical stability criterion, such as the Courant-Friedrichs-Lewy (CFL) criterion will dictate the maximal values that $\Delta t/\Delta x$ can take. In this case the criterion is defined as

$$\frac{\Delta t}{\Delta x}\max|f'| \leq 1 \tag{2.29}$$

2.3.3 Comparing the analytical and numerical solutions

Two main factors need to be considered when comparing the analytical and numerical solutions, stability and accuracy. In general the analytical solution will be considered exact and stable while the numerical solution will depend on the grid and time-step refinement.

To illustrate the effect of grid cell size on the frontal advance solution, three grid refinement cases are run. In Figure 5 the three cases are shown in A, B and C, with the blue curve representing the numerical solution, while the red curve indicates the analytical solution (the exact solution). Δx values are varied while all other parameters remain constant. The final graph, D, shows total recovery as a function of time for all three numerical solutions.

In figure C we can observe that by applying an appropriate grid increment the accuracy of the numerical solution is comparable with that of the exact solution. The stability of the numerical solution will rely on the stability criterion and the solution will remain stable if an appropriate

Δt value is chosen. The algorithm used in this case will automatically select a Δt value such that the stability criterion is satisfied.

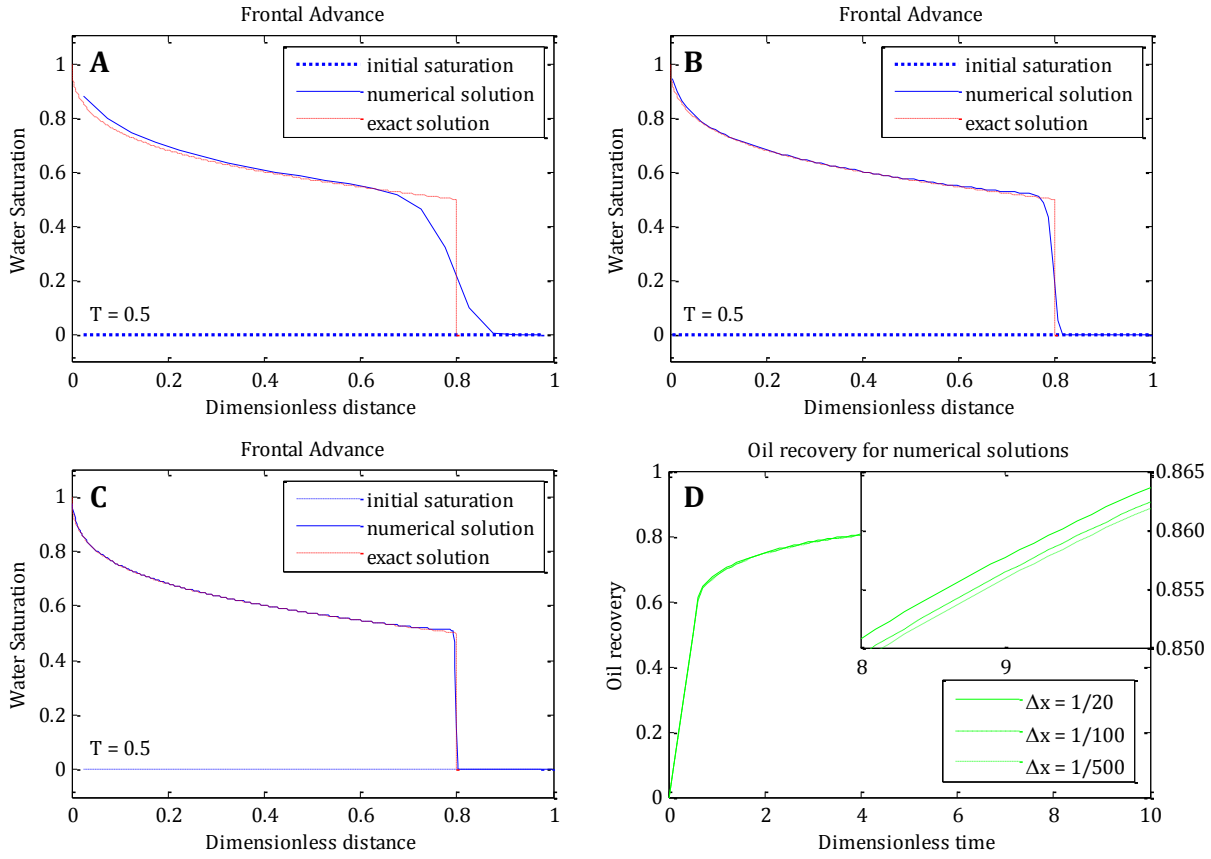

Figure 6: Plots comparing the analytical solution to the numerical solution. All cases use identical input parameters; M=0.5, no=4 and nw=2. The three first cases (A, B and C) are comparisons between analytical solution and numerical solutions for varying grid refinement in the x domain. In D oil recoveries for different numerical solutions are compared, where the fine grid is assumed approximately equal to the exact solution. See Appendix A for other input parameters.

2.4 Oil Recovery

The recovery efficiency can be defined as the amount of produced oil divided by the oil volume originally present in the reservoir. Before breakthrough, the amount of produced oil will be the same as the amount of injected water. And since t_D represents PV's injected, it will also represent the fraction of oil recovered.

After breakthrough, the average water saturation, $\bar{S}$, can be used to find the recovery given by the expression

$$N_p = \frac{(\bar{S} - S_{wi})A\varphi L}{B_o} \tag{2.30}$$

where S_{wi} is initial water saturation and B_o is formation volume factor for oil, and for our case are assumed equal to 0 and 1 respectively. Average water saturation can be found using the Welge equation [4]

$$\bar{S} = S^* + t^*(1 - f^*) \tag{2.31}$$

where S^* is the water saturation at $x = 1$, f^* is fractional flow when $x = 1$ and t^* is the dimensionless time required to propagate saturation S^* from the start ($x = 0$) to end ($x = 1$) of the system.

Alternately we can use the integral

$$N_p = \frac{\int_0^1 [S(x,t) - S_{wi}(x)]dx}{\int_0^1 [1 - S_{wi}(x)]dx}$$

This equation is used in the numerical modelling .

3 Effects on reservoir performance

In this part of the thesis we will look at some of the key concepts that influence reservoir performance in a BL model.

3.1 Fractional flow

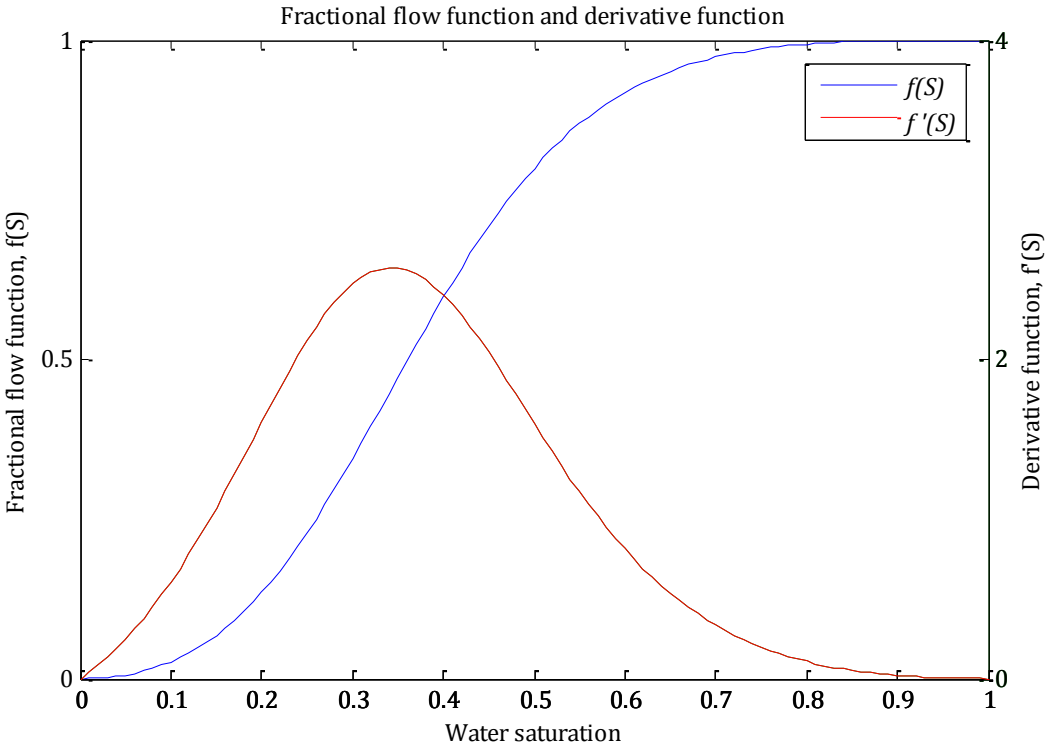

Figure 7: Fractional flow function and its derivative. See Appendix A for other input parameters.

The fractional flow function describes the volumetric fraction of water in a two-phase flow process [5]. This function can be defined as the volumetric rate of water q_w relative to total volumetric rate q:

$$f = \frac{q_w}{q} \tag{3.1}$$

where $q = q_w + q_o$, and q_o is the volumetric rate of oil. These rates can be expressed using two-phase Darcy flow:

$$q_l = -\frac{kk_{rl}A}{\mu_l}\left(\frac{\partial p_l}{\partial x} + \rho_l g \sin\alpha\right), \qquad l = o, w \tag{3.2}$$

Introducing the two phase capillary pressure term, $P_c = p_o - p_w$, we find an expression for q

$$q = -\frac{kk_{rw}A}{\mu_w}\left(\frac{\partial p_w}{\partial x} + \rho_w g \sin\alpha\right) - \frac{kk_{ro}A}{\mu_o}\left(\frac{\partial p_w}{\partial x} + \frac{\partial P_c}{\partial x} + \rho_o g \sin\alpha\right) \tag{3.3}$$

Solving (3.3) for the pressure gradient $\frac{\partial p_w}{\partial x}$ we get

$$\frac{\partial p_w}{\partial x} = \frac{-\frac{q}{A} - \frac{kk_{ro}}{\mu_o}\frac{\partial P_c}{\partial x} - k\left(\frac{k_{rw}}{\mu_w}\rho_w + \frac{k_{ro}}{\mu_o}\rho_o\right) g \sin\alpha}{k\left(\frac{k_{rw}}{\mu_w} + \frac{k_{ro}}{\mu_o}\right)} \tag{3.4}$$

and inserting this result into (2.30) gives a new expression for the volumetric rate of water

$$q_w = \frac{\frac{kk_{rw}A}{\mu_w}}{k\left(\frac{k_{rw}}{\mu_w} + \frac{k_{ro}}{\mu_o}\right)}\left[\frac{q}{A} + \frac{kk_{ro}}{\mu_o}\left(\frac{\partial P_c}{\partial x} - \Delta\rho g \sin\alpha\right)\right] \tag{3.5}$$

The generalized form of the fractional flow function can then be written as

$$f = \frac{1 + \frac{kk_{ro}A}{\mu_o q}\left(\frac{\partial P_c}{\partial x} - \Delta\rho g \sin\alpha\right)}{1 + \frac{\mu_w}{\mu_o}\frac{k_{ro}}{k_{rw}}} \tag{3.6}$$

For the BL case, with horizontal flow and zero capillary pressure, the fractional flow function can be expressed in a simpler form

$$f = \frac{1}{1 + \frac{\mu_w}{\mu_o}\frac{k_{ro}}{k_{rw}}} \tag{3.7}$$

which is a rewritten form of the expression given in equation (2.14).

Since viscosity is assumed to be constant it is practical to use a viscosity ratio $M = \mu_w/\mu_o$, and used in the expression above gives

$$f = \frac{1}{1 + M\frac{k_{ro}}{k_{rw}}} \tag{3.8}$$

Alternatively, mobility ratio could be used, which is useful when involving calculations related to displacement processes. Mobility ratio, M^*, can be defined as the mobility of a displacing fluid relative to that of a displaced fluid:

$$M^* = \frac{k_{rD}/\mu_D}{k_{rd}/\mu_d} = \frac{1}{M}\frac{k_{rD}}{k_{rd}} \tag{3.9}$$

where subscript D represents the displacing fluid and subscript d represents the displaced fluid. Related to a two-phase water-flood process the water will displace the oil [4].

In general the idea in a mobility control process is to increase water viscosity and thereby increase the viscosity ratio (or lower the mobility ratio) with the aim to achieve a more stable front and hence more efficient volumetric sweep. This can be achieved by manipulating the viscosity of the displacing fluid. Enhanced oil recovery processes involving viscosity control will not be the focus of this thesis; instead, viscosity will be discussed in terms of viscous properties of the fluids present in the reservoir.

Relative permeability can be described as a function of water saturation, and has been defined using Corey type oil and water relative permeability curves. These functions can be defined as

$$k_{rw} = (S_{wn})^{n_w}, \qquad k_{row} = (1 - S_{wn})^{n_o} \tag{3.10}$$

where n_w and n_o are the Corey exponents. The concept of relative permeability will be discussed in more detail in Chapter 3.2.

3.1.1 Studying the effect of viscosity ratio

To illustrate how a change in viscosity will effect the fractional flow function and consequently the rate of recovery, three scenarios are run as seen in Figure 8. In all three cases the relative permeabilities remain unchanged, using Corey exponents $n_w = 2$ and $n_o = 3$, while the viscosity ratio is varied using $M = (0.1, 0.5, 1.0)$.

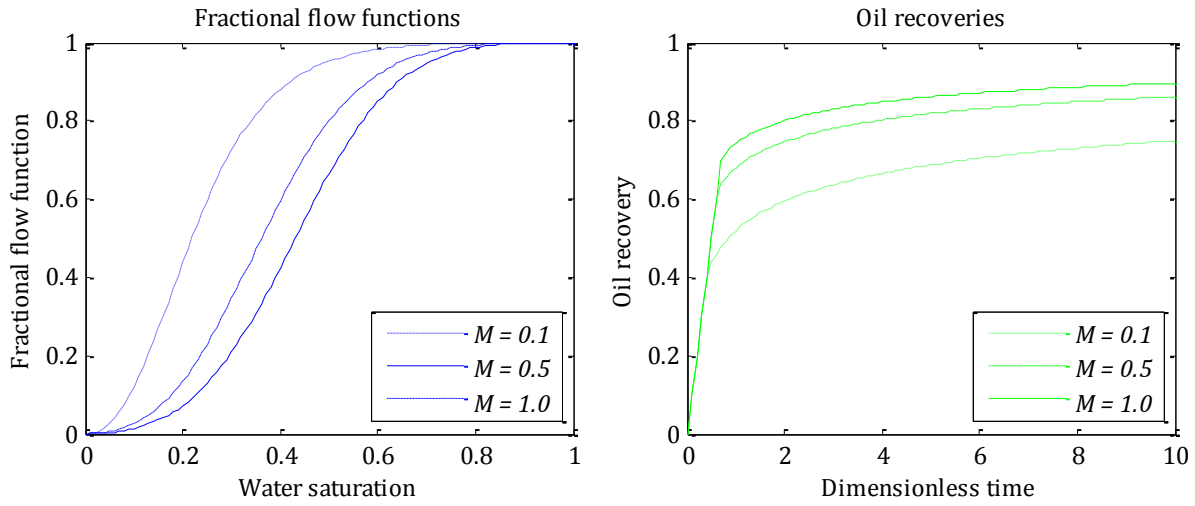

Figure 8: Plots showing fractional flow functions and oil recoveries for different viscosity ratios $M = (0.1, 0.5, 1.0)$. Relative permeabilities are defined using Corey exponents $n_w = 2$ and $n_o = 3$. Left: fractional flow functions. Right: oil recoveries. See Appendix A for other input parameters.

From the figure we observe that changes in viscosity ratio will effect the shape of the fractional flow function by skewing it to the right for increasing values and to the left for decreasing values. It can also be observed that these changes effect the rate of recovery, with the higher viscosity value ($M = 1.0$) resulting in an oil recovery efficiency close to 85% after approximately one injected PV. On the other hand, the scenario using the lowest viscosity value ($M = 0.1$) requires approximately nine injected PV's to recover the same amount. This implies that changes in viscosity ratio effect the rate at which a recovery is achieved, not recovery efficiency itself. The overall recovery efficiency relies on residual oil saturation which, for an idealized case, would be equal to zero, and eventually lead to100% oil recovery.

3.2 Relative permeability

The concept of relative permeability k_{rl} is used to relate absolute permeability k to effective permeability k_{el}, and can be expressed as:

$$k_{el} = k_{rl} \cdot k \tag{3.11}$$

While absolute permeability is a constant property of a porous medium related to a single phase flowing, the effective permeability will also be strongly tied to phase saturation. Laboratory experiments have shown that the sum of effective permeabilities are smaller than the absolute

permeability [5] [6]. This implies that relative permeability will depend on saturation distributions in a reservoir, fluid properties and reservoir characteristics, and is therefore strongly linked to viscous and capillary forces.

However, for mathematical modelling it is practical to consider relative permeabilities as functions of phase saturation only. Experimental work is carried out on core samples and relative permeability functions are constructed based on this data. A number of correlations exist where perhaps the most known are the Corey type curves that date back to the 1950's [7].

3.2.1 Rock wettability and relative permeability

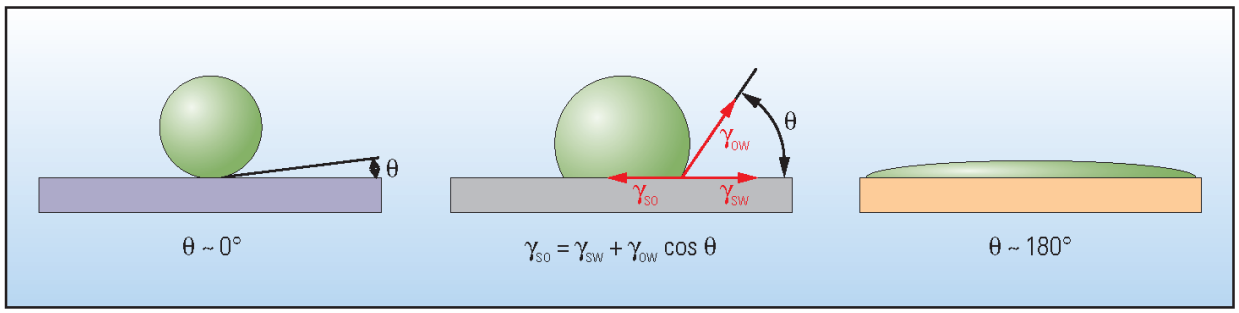

Figure 9: Contact angle (θ). An oil drop (green) is surrounded by water (blue).To the left a water-wet surface is illustrated with zero contact angle, while to the far right an oil-wet surface is shown having a contact angle of approximately 180°. The central figure shows an intermediate-wet surface with the contact angle resulting from a force balance among interfacial tension (γ) terms. Figure is taken from [8].

Wettability is the tendency of one fluid to preferentially stick to a rock surface in the presence of another fluid (see Figure 9), and plays an important role in reservoir performance and oil recovery [4] [5] [8]. For practical applications, reservoirs are often assumed to have a specific wetting state such as oil-wet, water-wet or intermediate-wet systems. In a strongly water-wet system we are describing a reservoir with a strong preference for water over oil, and oppositely so for a strongly oil-wet system. While these classifications are typical for core scale experiments the reservoir rocks seen at reservoir scale tend to be more complex and heterogeneous in nature [8]. This gives rise to a classification called mixed-wet. This classification describes a system with inhomogeneous wetting, where for example parts of the reservoir might have a saturation history different than that of other parts of the same reservoir. This could then give rise to both oil-wet and water-wet areas in the same reservoir.

Note that intermediate-wet or neutral-wet reservoirs are defined as wetting systems that have no preference between oil and water, while the mixed-wet reservoirs will have varying wetting preference throughout the reservoir. In Figure 10 water-wet, oil-wet and mixed-wet reservoirs have been illustrated.

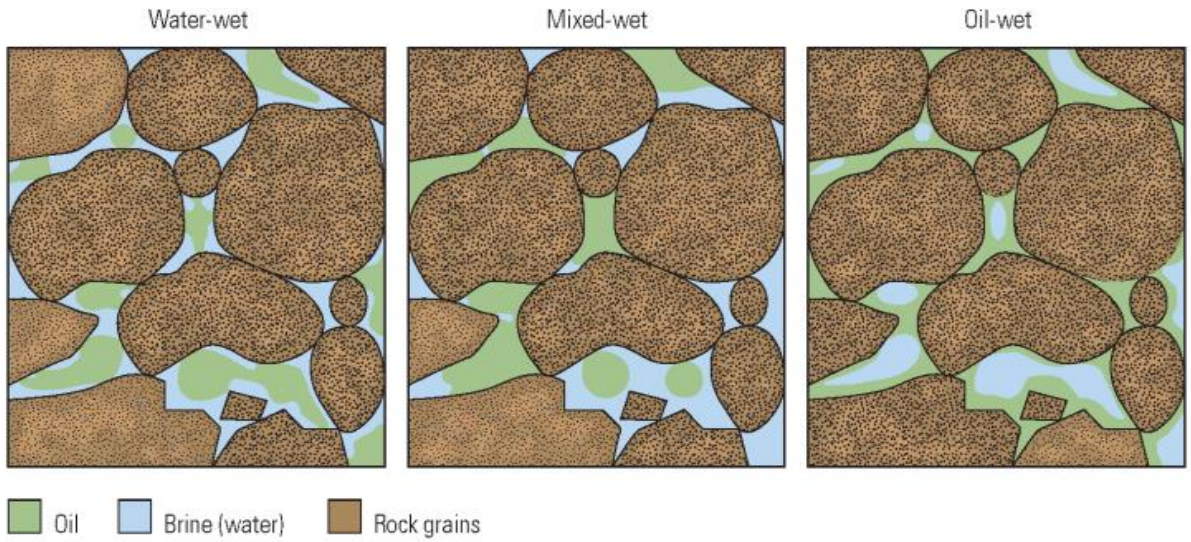

Figure 10: Wettability in pores. The figure shows three wettability cases; water-wet (left), mixed-wet (centre) and oil-wet (right). Note that all three conditions shown have similar saturations of water and oil. Figure is taken from [8].

In the literature it has been reported that there is interdependence between wettability, capillary pressure and relative permeability [4] [5] [8]. Both relative permeability and capillary pressure data from flooding of cores show a dependency on wetting conditions. This relationship is illustrated in Figure 11, where we show a set of relative permeability and capillary pressure curves for water-wet and mixed-wet systems. In the figure capillary pressure is shown using an imbibition curve and a set of drainage curves. Since most reservoirs are considered initially water wet [8], the primary drainage curve (dotted line) will typically be related to the initial migration of oil. In this case a core will initially be filled with water (wetting phase) which is displaced by oil (non-wetting phase). Similarly secondary drainage (dashed line) will describe secondary processes involving oil displacing water. On the other hand, the imbibition curve will describe behaviour related to water displacing oil.

In Figure 11 we see relative permeability curves that relate to corresponding capillary pressure curves. From these curves we can clearly see that the end point relative permeability values

change from one wetting condition to the next. In the case of mixed-wet conditions, this change results in decreased oil flow performance while water flow happens more readily. As will be shown later in section 3.2.4, and when discussing the Low Salinity Model in Chapter 5, this change in flow characteristics can have an impact on flow performance and oil recovery. Thus a proper understanding of relative permeability and representative wetting conditions is important. Note also that while capillary pressure has been neglected from a modelling perspective, it will still be represented through its relationship to relative permeability and wettability and thus only in part neglected.

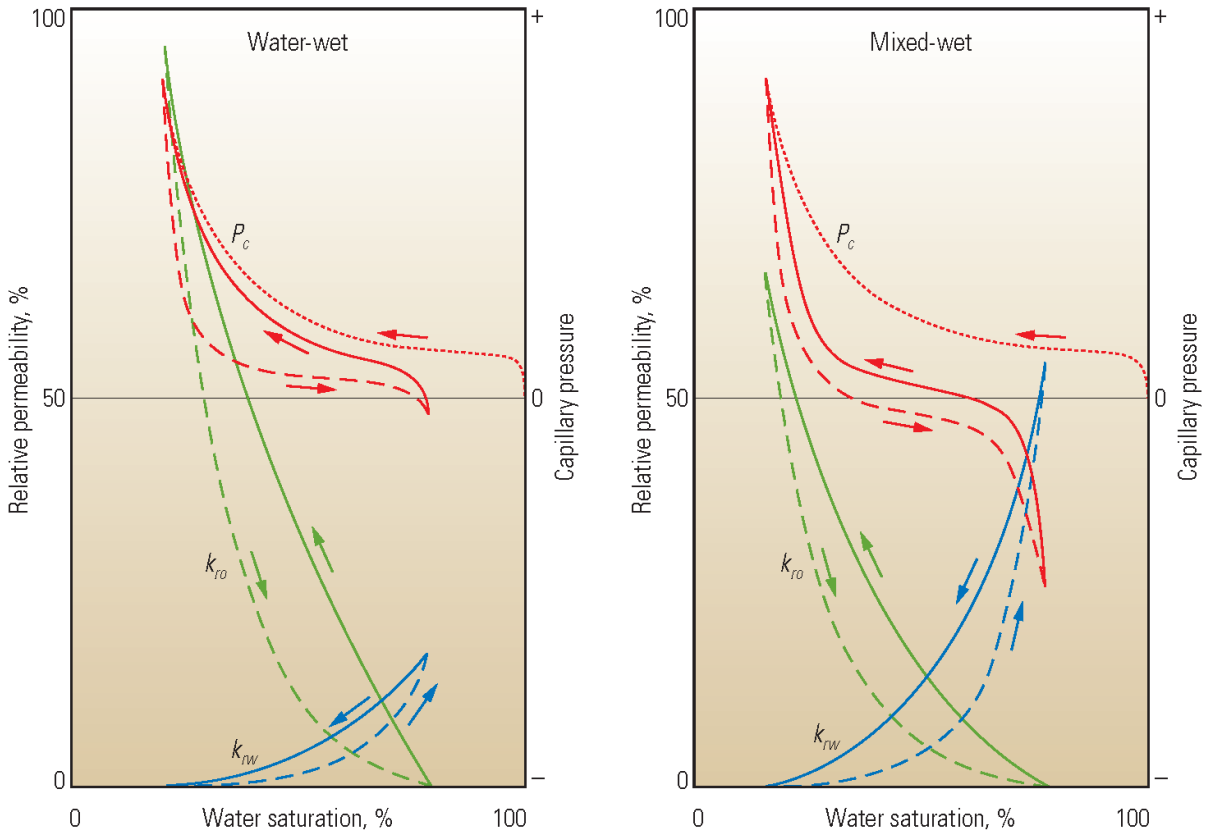

Figure 11: Capillary pressure and relative permeability for water-wet and mixed-wet conditions. The red curves show drainage (dotted and dashed) curves and an imbibition curve for capillary pressure, while relative permeability curves are shown in green for oil and blue for water. Note that the primary drainage curve is the same for both wetting conditions since most reservoirs are considered to be water-wet at time of oil migration. The figure is taken from [8].

3.2.2 Corey relative permeability

Introducing end point relative permeability's KRW (water), KRO (oil) and normalized water saturation S_{wn} the Corey water and oil relative permeabilities are expressed as

$$k_{rw} = KRW(S_{wn})^{n_w}, \qquad k_{row} = KRO(1 - S_{wn})^{n_o} \tag{3.12}$$

where n_w is the Corey water exponent, n_o is the Corey oil exponent and normalised water saturation is given by

$$S_{wn} = \frac{S_w - S_{wi}}{1 - S_{wi} - S_{or}}, \tag{3.13}$$

The parameters; S_{wi} and S_{or} represent initial water saturation and residual oil saturation. Although previous sections of this thesis have defined a water saturation interval that lies between 0 and 1, a more precise description should include end point saturations where $0 \leq S_{wn} \leq 1$ and $S_{wi} \leq S_w \leq 1 - S_{or}$.

3.2.3 LET relative permeability

While the Corey relative permeability functions are used extensively within industry, they arguably have limited application. An alternate correlation (LET) is given by Lomeland et al. [9], where they express water and oil relative permeabilities as

$$k_{rw} = KRW \frac{(S_{wn})^{L_w^o}}{(S_{wn})^{L_w^o} + E_w^o(1 - S_{wn})^{T_w^o}} \tag{3.14}$$

$$k_{row} = KRO \frac{(1 - S_{wn})^{L_o^w}}{(1 - S_{wn})^{L_o^w} + E_o^w(S_{wn})^{T_o^w}} \tag{3.15}$$

The parameters; KRW, KRO and S_{wn} are described as having physical meaning, identical to those used in the Corey expressions. The remaining parameters L_w^o, E_w^o, T_w^o, L_o^w, E_o^w and T_o^w are used as descriptive parameter, with L-values representing the lower part of the curves, T-values representing the top, and E-values describing the position of the slope.

According to Lomeland et. al., the number of descriptive parameters used in the LET model gives a higher degree of flexibility, giving better fit to experimental data compared to conventional correlations. In Figure 12 oil and water relative permeability functions are shown, comparing LET, Corey and Chierici type curves to a set of experimental data.

Of special interest is s-like behaviour seen for oil relative permeability data, at small water saturations values. It is suggested that this s-behaviour relates to wettability, and is probably a result of complex interaction between wettability, pore shape and pore-size [9]. From the figure we note that the LET correlation is able to account for this behaviour to a larger degree than the other correlations shown.

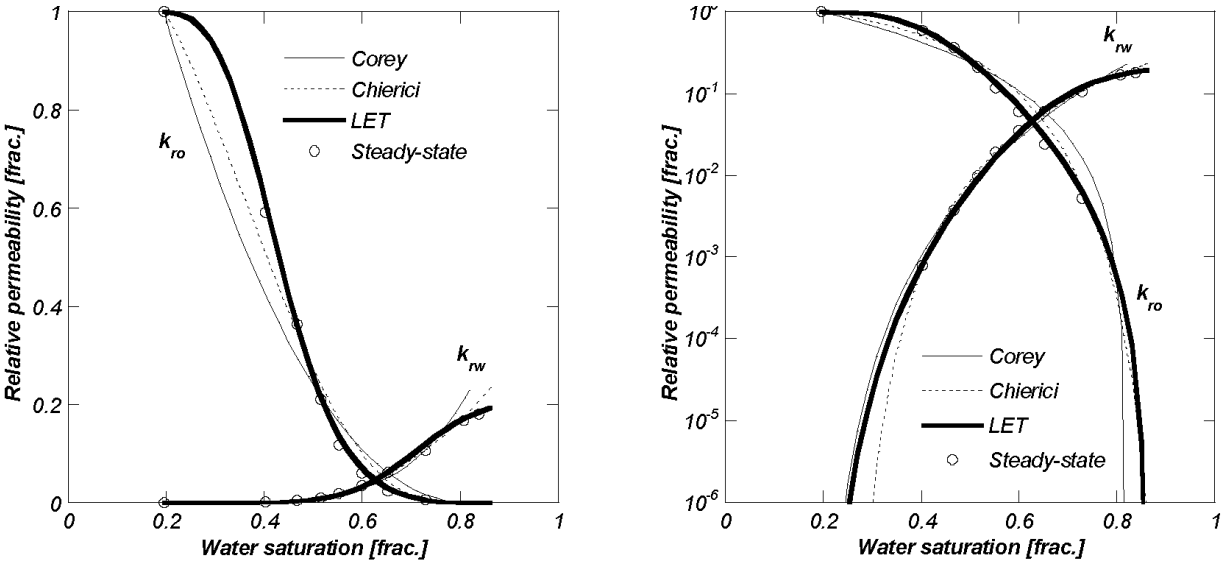

Figure 12: Relative permeability correlation comparison. Corey, Chierici and LET type relative permeability functions are fitted to a set of experimental data. Note that the left figure shows a lin-lin comparison, while the left figures shows a log-lin comparison. The figure is taken from [9].

3.2.4 Studying the effect of relative permeability

In this section we will study the effect of relative permeability on the frontal advance solution, and consequently the effect on recovery.

As a first step we will study the effect of wettability on the frontal advance solution. In this example we have simulated water-wet and mixed-wet systems, based on Figure 11. The Corey-type functions have been used to create relative permeabilities that are approximate matches to

those shown in the figure, with parameters supplied in Appendix A. In Figure 13 we show these relative permeability curves with their respective fractional flow functions.

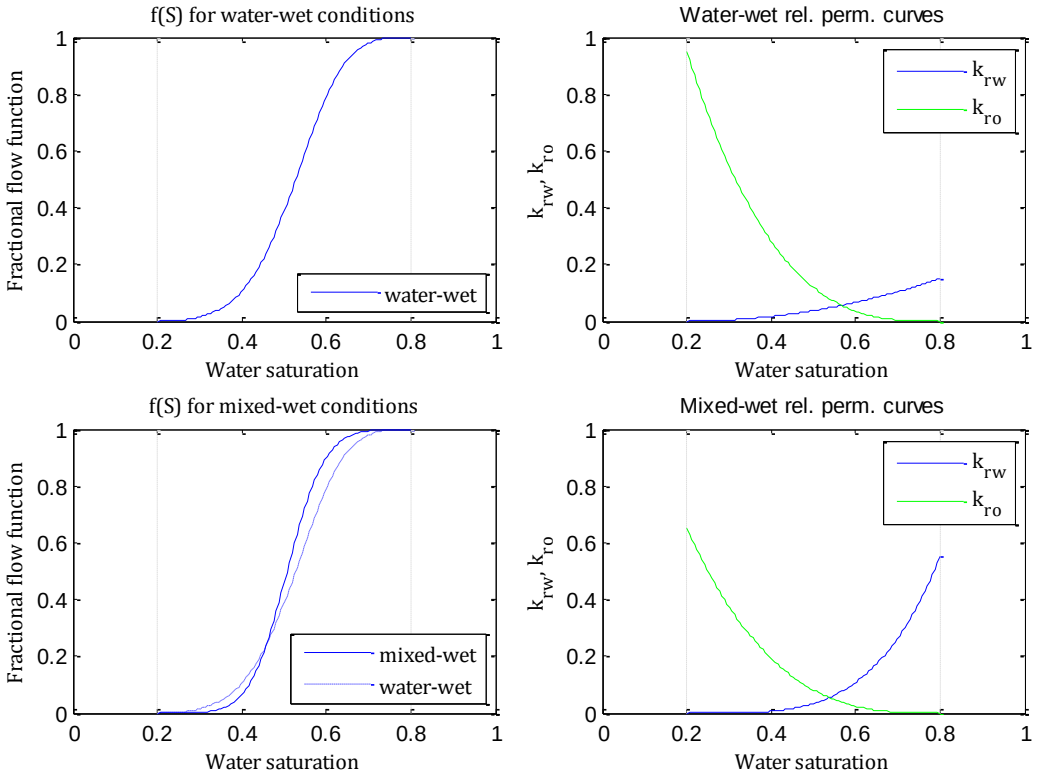

Figure 13: Plots showing fractional flow and realtive permeabilities for water-wet and mixed-wet systems. See Appendix A for other input parameters.

In Figure 14 we show the frontal advance solutions for both wetting conditions. We note that the mixed-wet conditions result in a faster flood front which should result in earlier water breakthrough and reduced oil recovery, as seen in Figure 15.

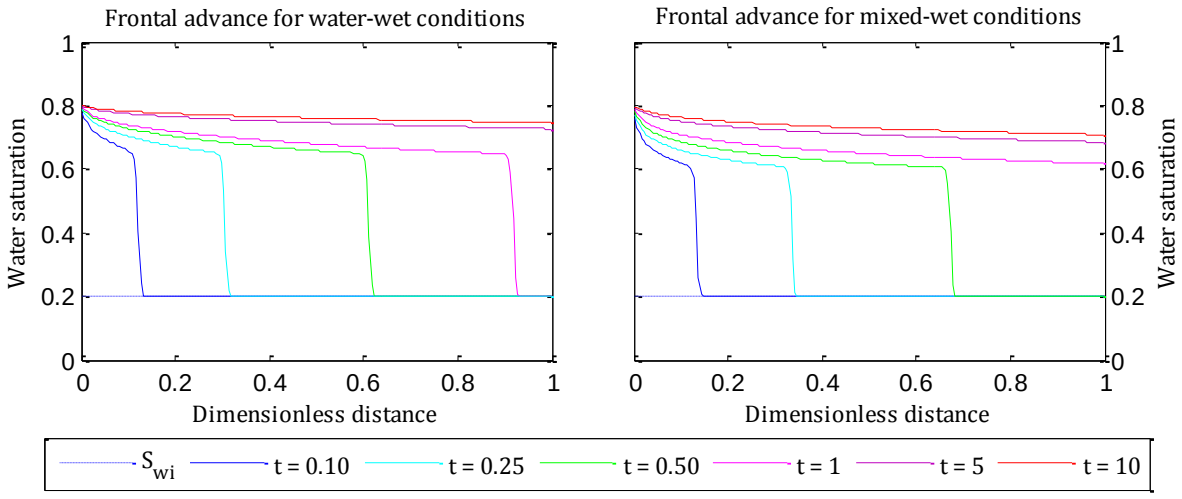

Figure 14: Plots showing frontal advance comparison for water-wet and mixed-wet condition. See Appendix A for other input parameters.

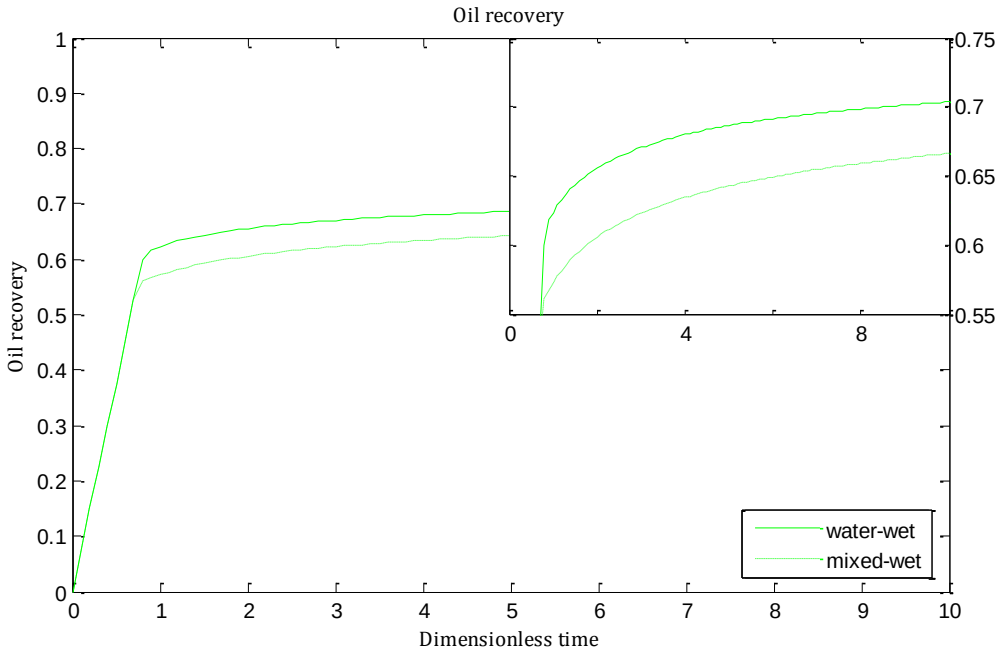

Figure 15: Oil recovery for water-wet and mixed-wet conditions. See Appendix A for other input parameters.

In the next example two sets of relative permeability functions have been created using Corey and LET type correlations, as seen in Figure 12. Lacking experimental data, the work done by Lomeland et. al. [9] has been approximated in order to construct these functions as shown in Figure 16. We assume that these functions are representative of water-wet sandstones, and represent a best fit to the data presented. It is also assumed that a LET type correlation gives a more accurate fit to experimental data.

In Figure 18 the frontal advance solutions for both correlation types are shown, using the five time increments: 0.1, 0.3, 0.6, 0.9 and 10. From the figure we can note that the difference in shape between the two type-curves effects both shape and front speed, as is especially apparent when considering the solution at $T = 0.6$.With a higher flood front speed for the LET solution we should expect an earlier water breakthrough and hence lower oil recovery than for the Corey solution. In Figure 18, showing oil recovery as a function of time, this is illustrated by the two solutions and giving an oil recovery difference of 5%, at $T = 0.9$. In other words the less accurate Corey functions results in a significant over estimate at early time values.

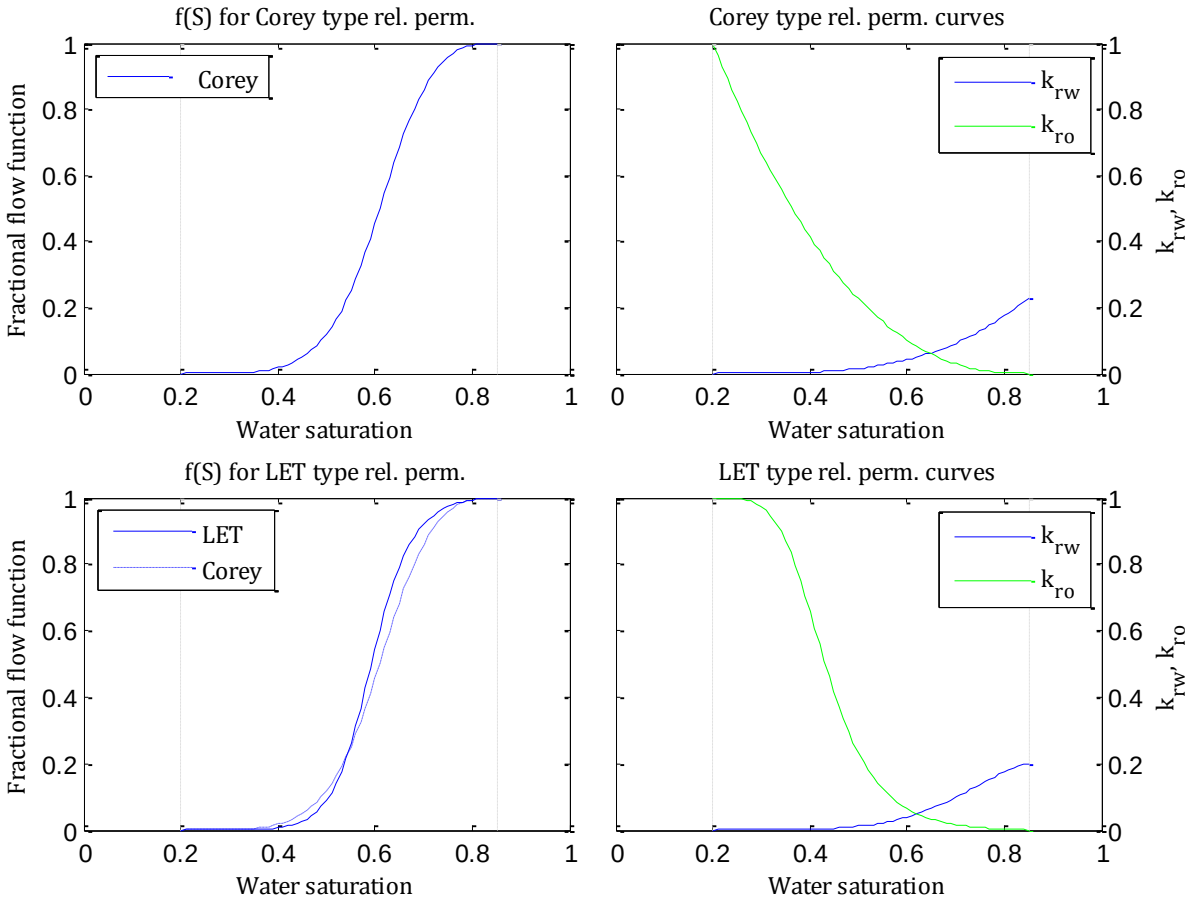

Figure 16:Comparison of Corey type relative permeability with LET type functions in a typical water-wet reservoir rock. See Appendix A for other input parameters.

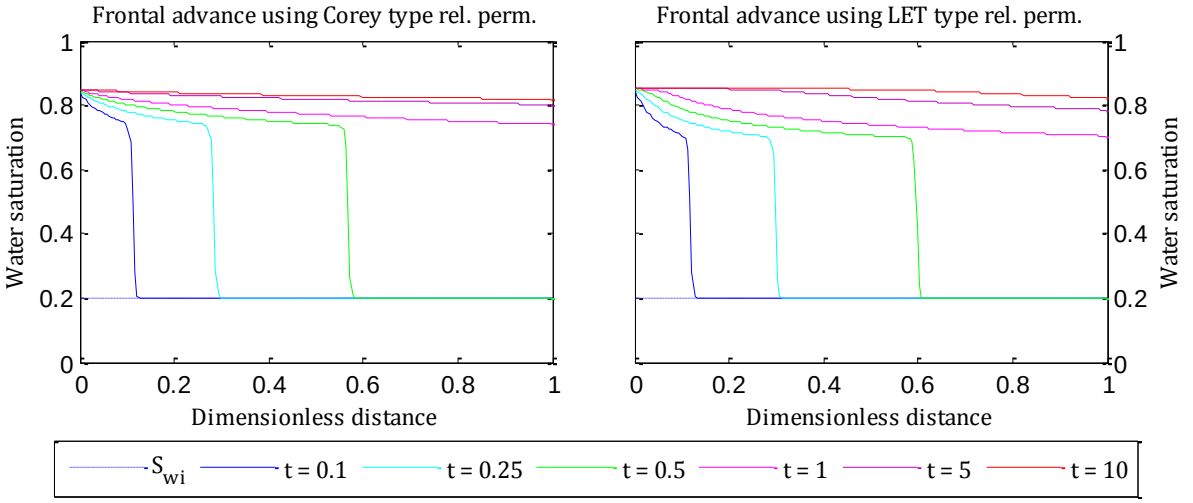

Figure 17: A comparison of LET and Corey-type permeability curves, studying the the impact of curve shape on frontal advance solutions. For each type-curve five cases are run, using dimensionless runtimes: 0.1, 0.3, 0.6, 0.9 and 10. See Appendix A for other input parameters.

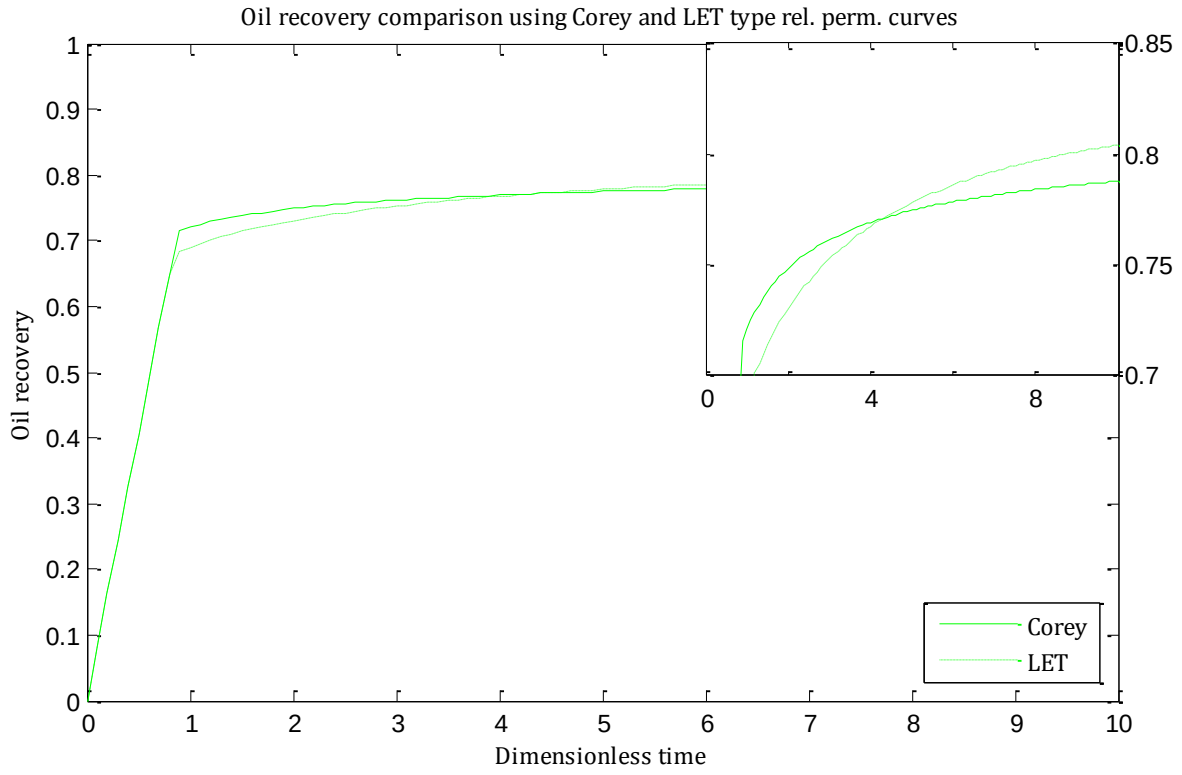

Figure 18: Displacement efficiency using Corey and LET type relative permeability's. See Appendix A for other input parameters.

4 Expanding the simplified Buckley-Leverett equation

When we first derived the BL equation in Chapter 2.2, we assumed that there was no gravity effect and capillary pressure was ignored. In this part of the thesis we will investigate how to include these in the model and how they will effect the immiscible displacement process.

4.1 Gravity

To study the effect of gravity on fluid flow in a 1D model, we introduce an inclination angle, α. As illustrated in Figure 19, the angle will result in a gravitational force component acting down dip. Depending on the direction of flow this will have different effects on the solution, and bears further investigation.

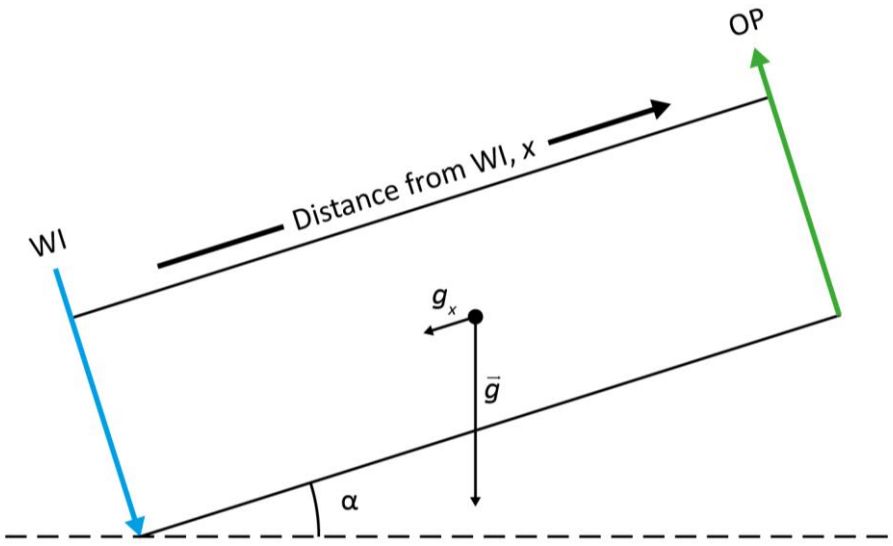

Figure 19: A tilted reservoir model, illustrating additional forces effecting the frontal advance equation

The extended BL equation will be derived using the two phase mass balance equations of the form

$$\varphi \frac{\partial S_l}{\partial t} - \frac{\partial}{\partial x}\left[\lambda_l \left(\frac{\partial p_l}{\partial x} + \rho_l g \sin\alpha\right)\right] = 0, \qquad l = o, w \tag{4.1}$$

Using a similar approach as for the normal BL equation, total flux is expressed as

$$u = -\lambda_w \left(\frac{\partial p_w}{\partial x} + g\rho_w \sin\alpha \right) - \lambda_o \left(\frac{\partial p_o}{\partial x} + g\rho_o \sin\alpha \right) \tag{4.2}$$

Capillary pressure is defined as

$$P_c = p_o - p_w \tag{4.3}$$

and by assuming P_c equal to zero the phase pressures are equal; $p_w = p_o$. Substituting the resulting pressure term from equation (4.2) into the water MBE, we get

$$\varphi \frac{\partial S_w}{\partial t} + \frac{\partial}{\partial x} \left\{ \lambda_w \left[\frac{u}{\lambda_t} + \left(\frac{\lambda_w \rho_w}{\lambda_t} + \frac{\lambda_o \rho_o}{\lambda_t} - \rho_w \right) g \sin\alpha \right] \right\} = 0 \tag{4.4}$$

which can be simplified to

$$\varphi \frac{\partial S_w}{\partial t} + u \frac{\partial}{\partial x} \left(\frac{1 - \frac{\lambda_o}{u} \Delta\rho g \sin\alpha}{1 + \frac{\lambda_o}{\lambda_w}} \right) = 0 \tag{4.5}$$

where $\Delta\rho = \rho_w - \rho_o$. Now considering the fractional flow function in (3.6) and ignoring capillary pressure we get

$$f = \frac{1 - \frac{\lambda_o}{u} (\Delta\rho g \sin\alpha)}{1 + \frac{\lambda_o}{\lambda_w}} \tag{4.6}$$

and substituting into the water MBE, gives the familiar BL equation

$$\varphi \frac{\partial S}{\partial t} + u \frac{\partial f}{\partial x} = 0 \tag{4.7}$$

where $S = S_w$.

It is convenient to gather all constant parameters into a dimensionless gravity term,

$$G = \frac{Ck\Delta\rho g \sin\alpha}{\mu_o u} \tag{4.8}$$

using the conversion factor $C = 8.356 \cdot 10^{-5}$ for parameters using the following units; k (mD), $\Delta\rho$ (kg/m^3), μ (cP), u (m/day). Using the gravity term, the fractional flow can be expressed as

$$f = \frac{1}{1 + \frac{\lambda_o}{\lambda_w}} - \frac{Gk_{ro}}{1 + \frac{\lambda_o}{\lambda_w}} \tag{4.9}$$

4.1.1 Investigating the effect of gravity

To study the effect of gravity on the frontal advance solution several scenarios have been run using different values of G. Among the physical parameters defining G, the inclination angle α will be used to investigate characteristic behaviour of fluid flow.

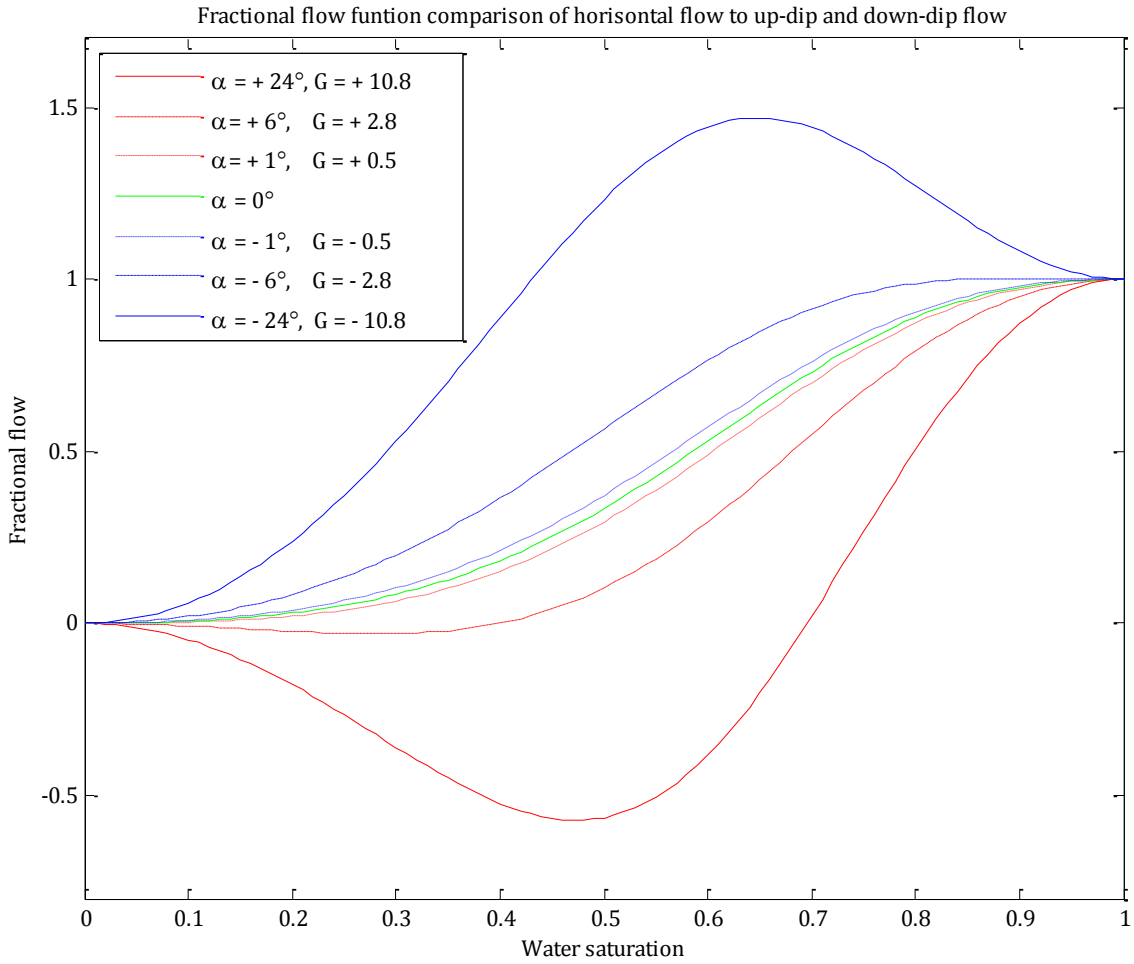

Figure 20: A comparison of fractional flow functions showing the effects of gravity. The gravity term (G) has been modified by only changing the inclination angle (α). See Appendix B for other input parameters.

In Figure 20 the difference between up-dip and down-dip flow is illustrated using the fractional flow function. In the seven cases shown in the figure the only parameter in G that has been

varied is the inclination angle α. The green curve represents a base case with zero dip, while the red curves represent up-dip flow with dip angles: 1˚, 6˚, and 24˚. Blue curves show the effect of down-dip flow using the same but opposite angles. Note that for down-dip flow the fractional flow curve attains values greater than 1.0, and negative values for up-dip flow. This relates to counter-current and co-current effects.

In a production setting the most common water flood scenario will involve frontal advance solutions for up-dip flow. Hence, the three up-dip flow scenarios shown in Figure 20 are used to solve for the saturation function. The results are computed for four time values: 0.1, 0.5, 1.0 and 5.0, and are displayed in Figure 21.

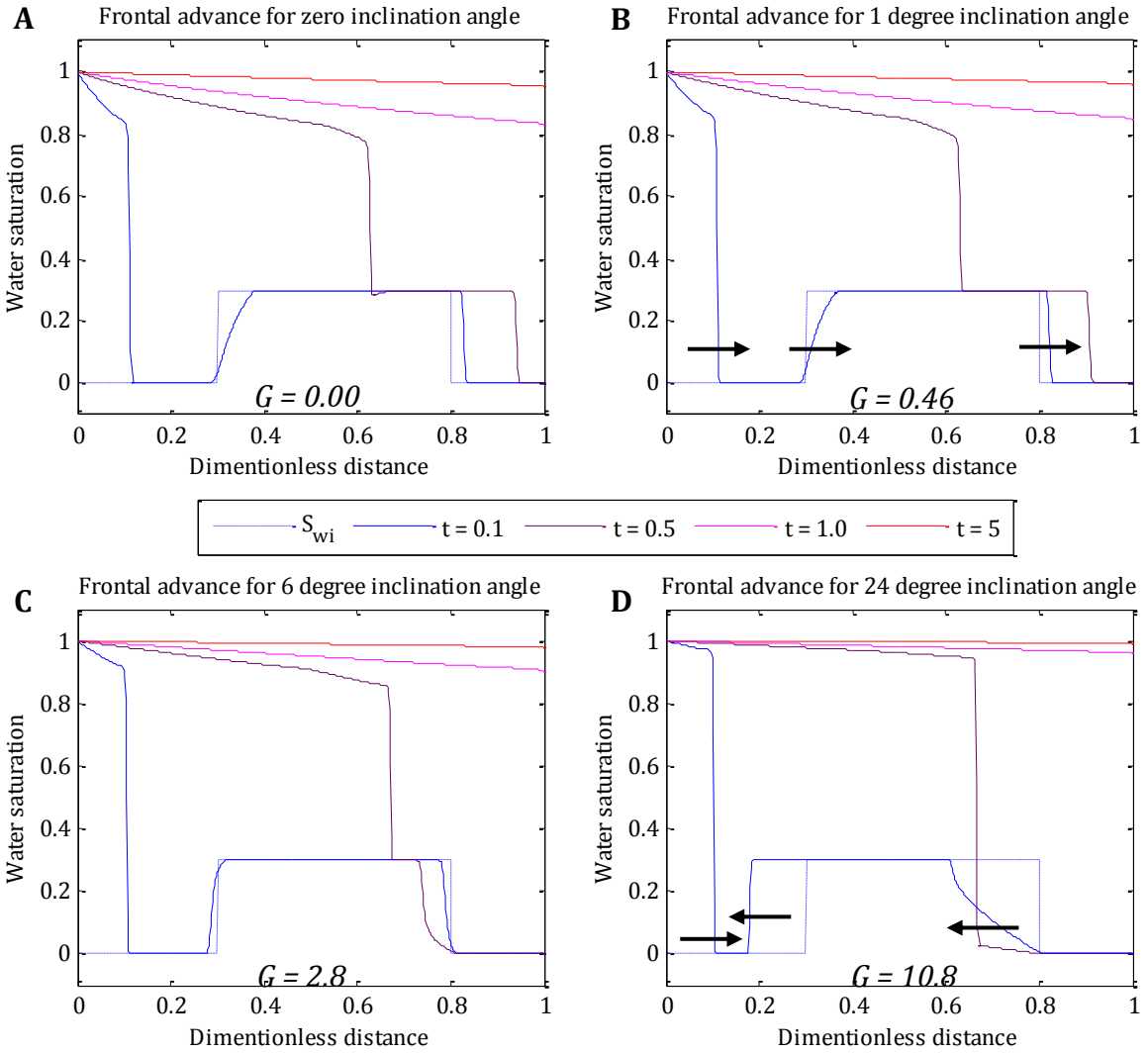

Figure 21: Comparison of co-current and counter-current effects due to gravity. Four cases are run using different values of G (corresponding to changing dip angles), and a zone in the x-domain containing higher initial water saturation. Arrows to the right indicate up-dip flow while arrows to the left indicate down-dip flow. See Appendix B for other input parameters.

To show the effects of gravity on flow behaviour, the initial water saturation is set to be non-zero in a portion of the reservoir. Studying the fluid movement in this zone we can see co-current and counter-current effects in the model. In Figure 21 arrows have been used in parts B and D to indicate direction of flow, with right arrow indicating up-dip flow. From part A we can observe co-current flow as expected in a horizontal reservoir, while C and D show counter-current flow due to gravity, increasing with the value of G. However, for small inclination angles and consequently small values of G (part B) we can see co-current behaviour, similar to that seen in part A.

With closer investigation of Figure 21 we observe that the saturation, at and behind the flood front, varies with G. Studying parts B and D we can see a clear difference between front heights for all time increments chosen, though this difference does decrease with time. This gives us better volumetric sweep of the reservoir for increasing positive values of G, as the oil recovery curves in Figure 22 show. Also note that time to breakthrough increases with G.

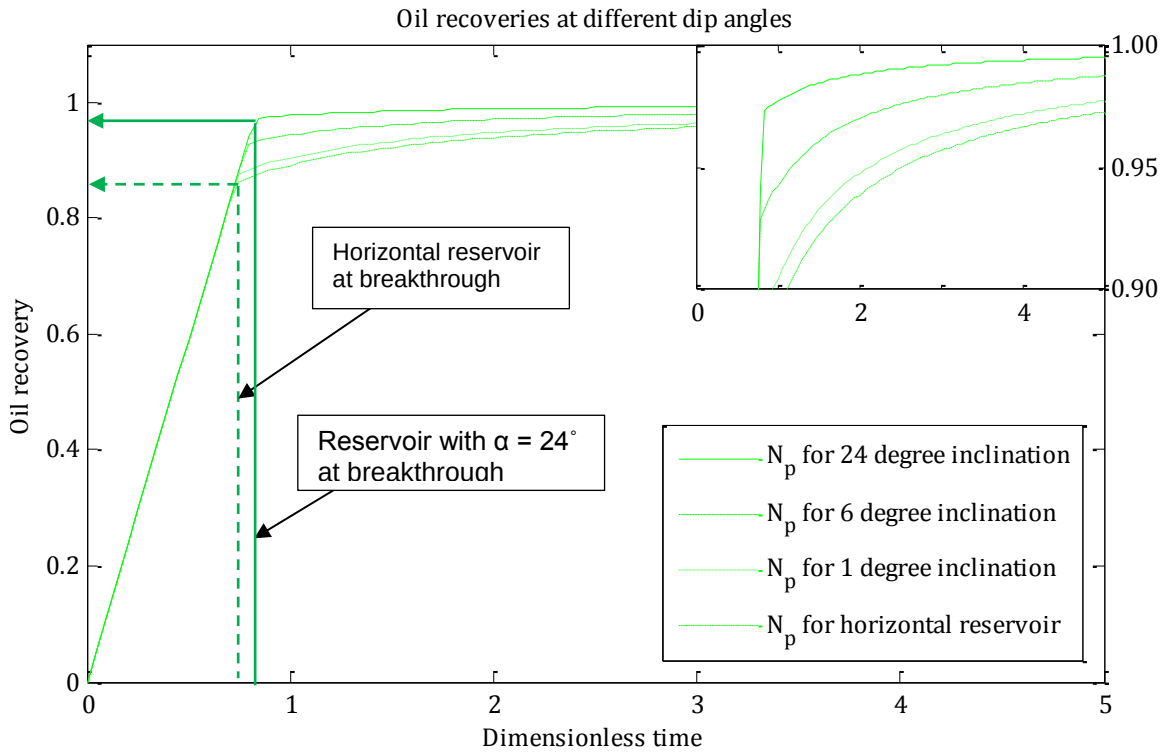

Figure 22: Oil recovery for up-dip flow comparisons. One horizontal flow case is compared with 3 up-dip flow scenarios using 1, 6 and 24 degree dip angles. See Appendix B for other input parameters.

4.2 Capillary Pressure

Capillary pressure (P_c) is defined as the pressure differential that occurs across the interface between two immiscible phases, such as oil and water [10]. In a reservoir system interaction between the fluids and the rock face are also important, and in such, dependent on the wettability of the system. In short Zolotukin et. al. [5] thus describes P_c as the molecular pressure difference between the wetting and non-wetting phase.

Considering a capillary tube set in a container filled with water and overlain by oil, as demonstrated in Figure 23, it can be shown that the capillary pressure is defined as

$$P_c = \frac{2\sigma_{ow}\cos\theta}{r} \tag{4.10}$$

where σ_{ow} is interfacial tension (IFT), r is the radius of the capillary, and θ is the contact angle (which relates to the wettability) [4] [5] [8].

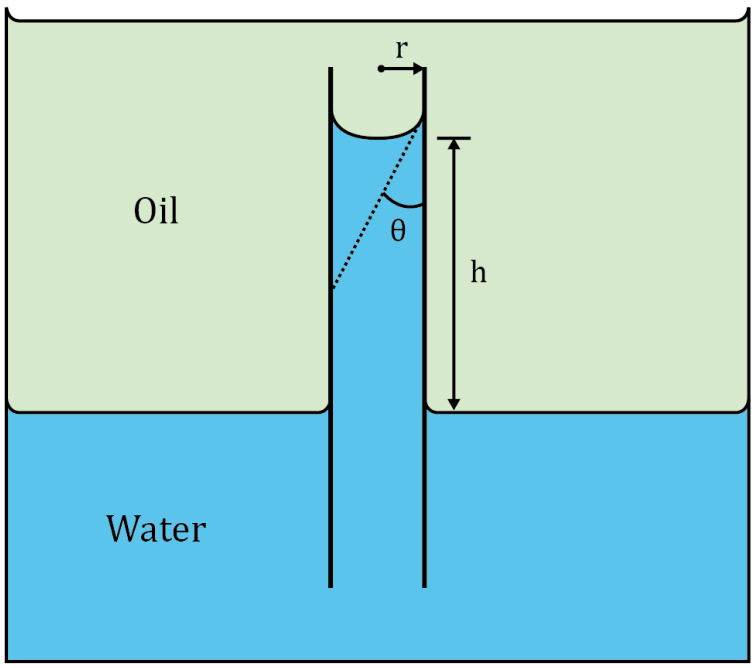

Figure 23: Illustration of capillary tube experiment

This experiment can be linked to saturation distributions and fluid contacts in a reservoir, though less significant in the case of a horizontal reservoir. There are a variety of other idealized

models describing the relationship between P_c, σ and r (capillary or pore radius), but these tend to be applicable on a smaller scale than that which is relevant in a production type setting. In such cases empirical correlations fitted to laboratory data are used more often.

Figure 24 has been generated using a correlation called LET; and displays a set of drainage and imbibition curves. As discussed in section 3.2, the drainage curves relate to the non-wetting phase (oil) which displaces the wetting-phase (water). Primary drainage relates to the initial filling of the reservoir, and hence the initial saturation distribution in the reservoir, while secondary drainage relate to later displacement processes. The imbibition curve describes processes where the wetting phase (typically water) displaces non-wetting phase (oil). The positive upper part of the imbibition curve represents spontaneous imbibition while the negative lower part describes forced imbibition. These relate to the processes involving increasing water saturation, where the forced imbibition could be tied to processes such as water flooding.

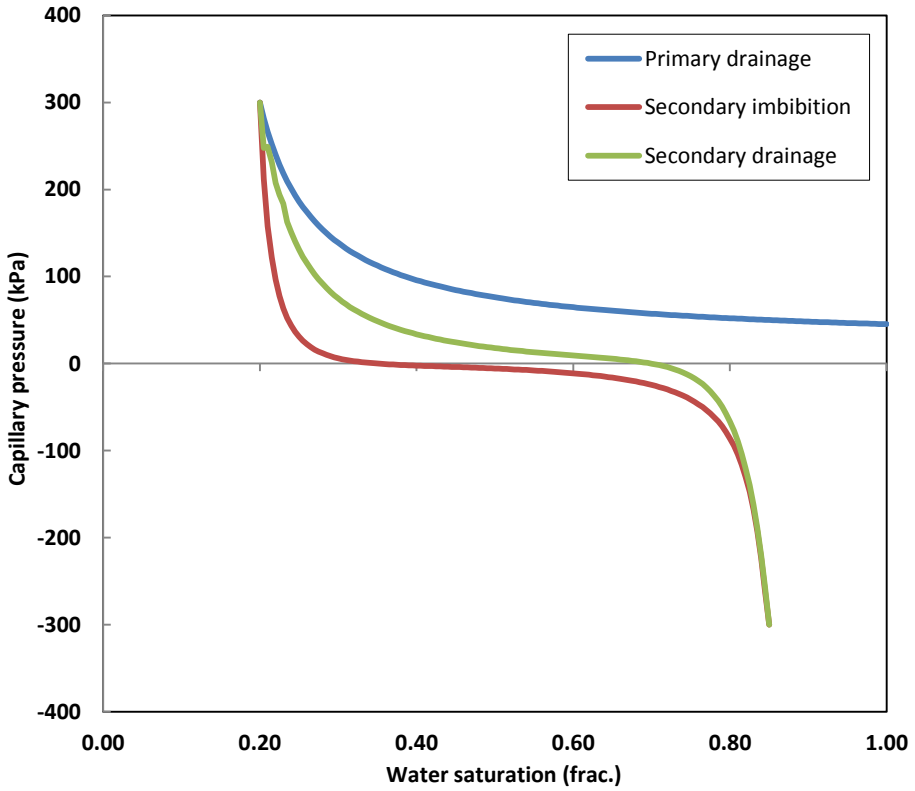

Figure 24: Basic capillary pressure curves. These examples are made using the LET-type capillary pressure functions.

There are a number of different capillary pressure correlations that can be used, among which the Leverett J-function [11], LET functions [12] and [13] are a few. In the remaining part of this chapter the LET type capillary pressure is used, and is defined as

$$P_c = \frac{P_c^{si}(1-S)^{L^{si}}}{(1-S)^{L^{si}} + E^{si}S^{T^{si}}} + \frac{P_c^{fi}(S)^{L^{fi}}}{S^{L^{fi}} + E^{fi}(1-S)^{T^{fi}}} \tag{4.11}$$

where P_c^{si} and P_c^{fi} are the maximum and minimum capillary pressures. The L, E and T parameters are similarly defined as the shape parameter used in the LET relative permeability functions (see section 3.2.3).

Similar to the discussion involving the LET type relative permeability functions, Lomeland et. al. suggest that this correlation has a greater degree of flexibility and arguably better fit to data. Alternately we could have used other capillary pressure correlations, such as the one suggested by Skjæveland et. al [13].

4.2.1 Deriving a general form of the Buckley-Leverett equation

Based on Chapter 4.1 we will now derive a general form of the BL equation including non-zero capillary pressure. Starting with equations (4.2) and (4.3) we can derive a water phase pressure term given by

$$\frac{\partial p_w}{\partial x} = -\frac{u + \lambda_o \frac{\partial P_c}{\partial x} + (\lambda_w \rho_w + \lambda_o \rho_o) g \sin\alpha}{\lambda_t} \tag{4.12}$$

which can be substituted into the water phase MBE from (4.1) to give

$$\varphi \frac{\partial S}{\partial t} + \frac{\partial}{\partial x}\left\{\lambda_w \left[\frac{u}{\lambda_T} + \frac{\lambda_o}{\lambda_T}\frac{\partial P_c}{\partial x} + \left(\frac{\lambda_w \rho_w}{\lambda_t} + \frac{\lambda_o \rho_o}{\lambda_t} - \rho_w\right) g \sin\alpha\right]\right\} = 0 \tag{4.13}$$

and simplified to

$$\varphi \frac{\partial S}{\partial t} + \frac{\partial}{\partial x}\left[\frac{u + \lambda_o \frac{\partial P_c}{\partial x} - G k_o}{1 + \frac{\lambda_o}{\lambda_w}}\right] = 0 \tag{4.14}$$

Considering the generalized form of the fractional flow function shown in Chapter 3.1, and using the gravity term G we get

$$f = \frac{1 + \frac{k k_{ro}}{\mu_o u}\left(\frac{\partial P_c}{\partial x}\right) - G k_{ro}}{1 + \frac{\lambda_o}{\lambda_w}} \tag{4.15}$$

which can be substituted into (4.13) to give the BL equation

$$\varphi \frac{\partial S}{\partial t} + u \frac{\partial f}{\partial x} = 0 \tag{4.16}$$

Again, it is convenient to introduce dimensionless constants and variables. In this case we use the constant ε and the pressure P_{cD}, as defined in equation (4.17).

$$\varepsilon = \frac{Kk}{\mu_o u}\frac{P_{c,ref}}{L} \quad and \quad P_{cD} = \frac{P_c}{P_{c,ref}} \tag{4.17}$$

Here ε is computed using the conversion factor $K = 8.52768 \cdot 10^{-3}$ when the following units are used; k (mD), $P_{c,ref}$ (bar), u (m/day), L (m) and μ_o (cP). Note that a reference pressure $P_{c,ref}$ is also introduced.

If we now use the previously defined dimensionless variable x_D in addition to ε and P_{cD}, equation (4.15) can be written as

$$f = \tilde{f}\left(1 + \varepsilon k_{ro}\frac{\partial P_{cD}}{\partial x_D} - G k_{ro}\right) \tag{4.18}$$

where

$$\tilde{f} = \frac{1}{1 + \frac{\lambda_o}{\lambda_w}} \tag{4.19}$$

which corresponds to the simplified form of the fractional flow function used in the initial BL equation.

Changing our notation, as done in Chapter 2.2.1, we use (4.16) and (4.18) to obtain the general BL equation in dimensionless form:

$$\frac{\partial S}{\partial t} + \frac{\partial}{\partial x}\left[\tilde{f}\left(1 + \varepsilon k_{ro}\frac{\partial P_{cD}}{\partial x} - G k_{ro}\right)\right] = 0 \tag{4.20}$$

To study the effects of capillary pressure the gravity term will be ignored in the remaining part of this chapter.

4.2.2 Numerical solution

When looking at the BL equation of the form given in equation (4.20) we note that it contains a second order derivative with respect to x, while previous cases have only held a first order derivative with respect to x. This introduces additional complexity when trying to solve the equation numerically.

Starting with equation (4.20) and using shorthand notation we have

$$\partial_t S + \partial_x \tilde{f} + \varepsilon \partial_x (a \partial_x P_{cD}) = 0 \tag{4.21}$$

where $a(S) = k_{ro}(S)\tilde{f}(S)$.

Using an explicit numerical scheme we get

$$\partial_t S = \tfrac{1}{\Delta t}\left(S_j^{n+1} - S_j^n\right) \tag{4.22}$$

$$\partial_x \tilde{f} = \tfrac{1}{\Delta x}\left(\tilde{f}_{j+\frac{1}{2}}^n - \tilde{f}_{j-\frac{1}{2}}^n\right) \tag{4.23}$$

$$\partial_x(a\partial_x P_{cD}) = \frac{1}{\Delta x}\left(a^n_{j+\frac{1}{2}}\partial_x P^n_{cD,j+\frac{1}{2}} - a^n_{j-\frac{1}{2}}\partial_x P^n_{cD,j-\frac{1}{2}}\right) \tag{4.24}$$

The a and P_c terms can be approximated using

$$a^n_{j+\frac{1}{2}} = \left(\frac{a^n_j + a^n_{j+1}}{2}\right), \qquad a^n_{j-\frac{1}{2}} = \left(\frac{a^n_{j-1} + a^n_j}{2}\right) \tag{4.25}$$

$$\partial_x P^n_{cD,j+\frac{1}{2}} = \left(\frac{P^n_{cD,j+1} - P^n_{cD,j}}{\Delta x}\right), \qquad \partial_x P^n_{cD,j-\frac{1}{2}} = \left(\frac{P^n_{cD,j} - P^n_{cD,j-1}}{\Delta x}\right) \tag{4.26}$$

Finally, we rewrite equation (4.21) and solve for timestep $n+1$ to get

$$S^{n+1}_j = S^n_j - \frac{\Delta t}{\Delta x}\left(\tilde{f}^n_{j+\frac{1}{2}} - \tilde{f}^n_{j-\frac{1}{2}}\right)$$

$$-\varepsilon\frac{\Delta t}{\Delta x^2}\left[\left(\frac{a^n_j + a^n_{j+1}}{2}\right)\left(P^n_{cD,j+1} - P^n_{cD,j}\right) - \left(\frac{a^n_{j-1} + a^n_j}{2}\right)\left(P^n_{cD,j} - P^n_{cD,j-1}\right)\right] \tag{4.27}$$

Note that $\tilde{f}^n_{j+\frac{1}{2}}$ and $\tilde{f}^n_{j-\frac{1}{2}}$ are solved using the MUSCL schema, as mentioned in Section 2.3.2. The inclusion of capillary pressure in the numerical model will give rise to stability issues. To keep numerical stability we therefore introduce an inner loop to the model, where Δt is automatically subdivided into smaller time units to make sure that the CFL criterion is satisfied. The criterion for the diffusion term is defined as

$$\varepsilon\frac{\Delta t}{\Delta x^2}\max\left|\left(\frac{a^n_j + a^n_{j+1}}{2}\right)P'_{cD}\right| \leq \frac{1}{2} \tag{4.28}$$

In practice this criterion will be most difficult to satisfy close to the end-point saturations S_{wi} and S_{or} where the capillary pressure has asymptotic behaviour.

4.2.3 Investigating the effect of capillary pressure

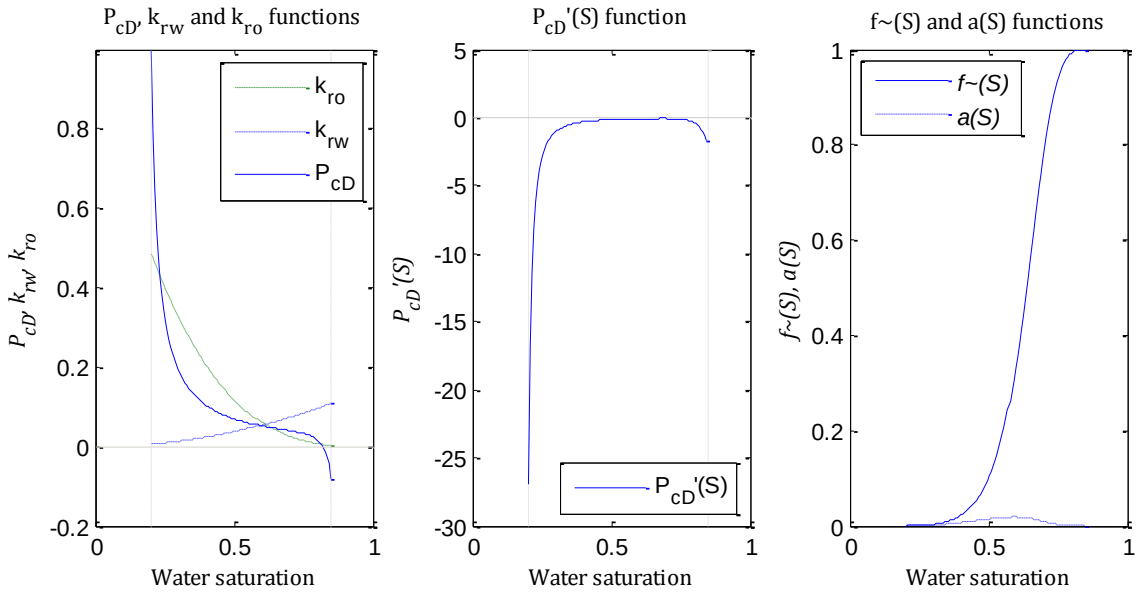

Figure 25: Various plots showing relevant functions. Left: Dimensionless capillary pressure imbibition curve plotted with water and oil relative permeability functions. Centre: The derivative of dimensionless capillary pressure with respect to S. Right: Plot of the simplified fractional flow function $\tilde{f}(S)$ and a(S) function. See Appendix C for other input parameters.

In Figure 25 we show dimensionless capillary pressure (imbibition) and relative permeability curves that are used in the frontal advance solution. The figure also shows the derivative of dimensionless capillary pressure with respect to water saturation, which is an important factor in the CFL criterion given in (4.28). The last plot shows the simplified fractional flow function $\tilde{f}(S)$ and the function $a(S)$ which are also factors in the CFL criterion.

To study the effect of capillary pressure, a number of cases have been run, using different values of the dimensionless constant ε. Four of the modelling results are presented in Figure 26, showing frontal behaviour for an increasing capillary pressure effect. The motivation for the choice of parameters defining ε, has been to compare core scale effects to reservoir scale effects. Since we have no direct access to measured reservoir data, the core data reported in [1] has been used. By changing the reservoir length L the core data has been scaled up to simulate reservoir scale conditions. The other input parameters that define ε can vary, and the dominating factor is expected to be L [5]. Table 1 in Appendix C gives ranges of ε values, where the other parameters have also been varied. On the basis of this table we have chosen the set of ε values used in these simulations (Figure 26 and Figure 27).

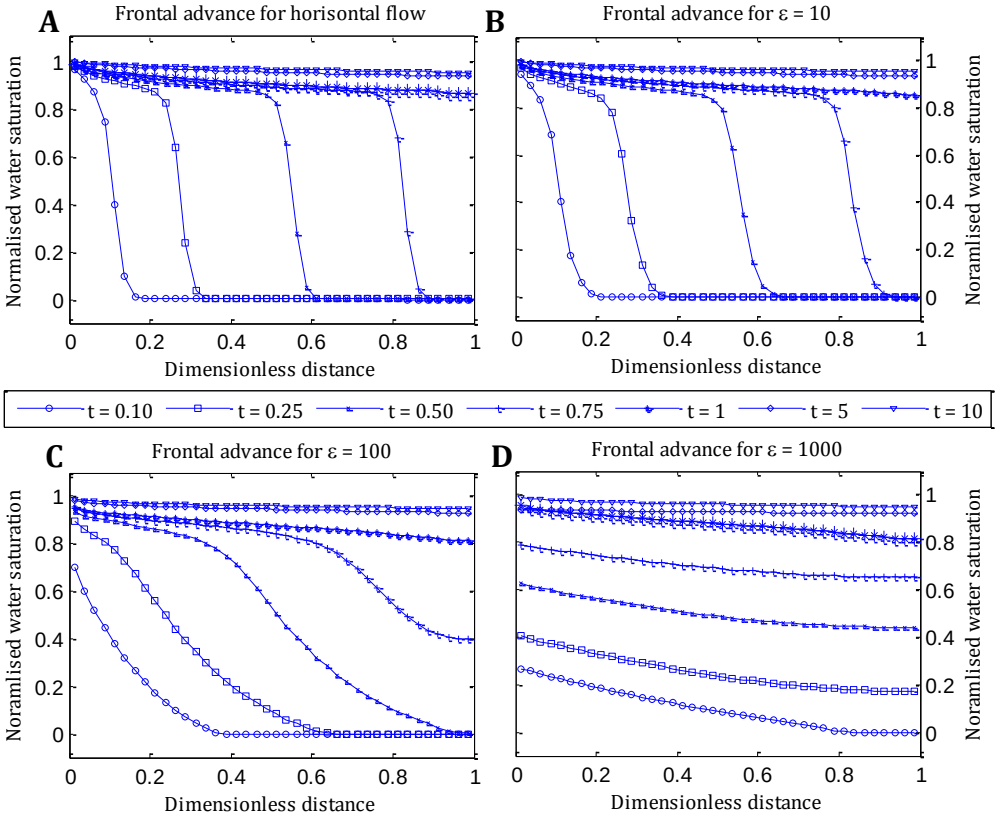

Figure 26: Plots showing frontal advance solutions including effects from capillary pressure. Note that these simulations are based on a model using only 40 grid cells in the x domain, which accounts for the slight smearing seen in A and will account for some of the smearing seen in part B, C and D. See Appendix C for other input parameters.

In Figure 26 we note strong capillary effects for the higher values of ε, as seen in C and D. These effects result in strong smearing of the shock front. Note that part of this smearing will be related to the grid resolution, since only 40 grid cells are defined in the x domain. Consequently, the smearing effects seen in A are purely related to numerical effects. From these results we would expect earlier water breakthrough for strong capillary effects, and hence lower oil recovery, as seen in Figure 27.

In general we note that severe capillary effects have a negative impact on oil recovery. However, considering the results above, we note that these effects seem to be most relevant at smaller scales and directly proportional to the length of the reservoir. As a consequence of this effect, it would be reasonable to assume that the capillary effects are very small in a production setting. The results are however more severe at core scale than was expected, which leads us to believe that there might be a scaling issue in the script used for the simulations, or some of the input parameter may not be representative.

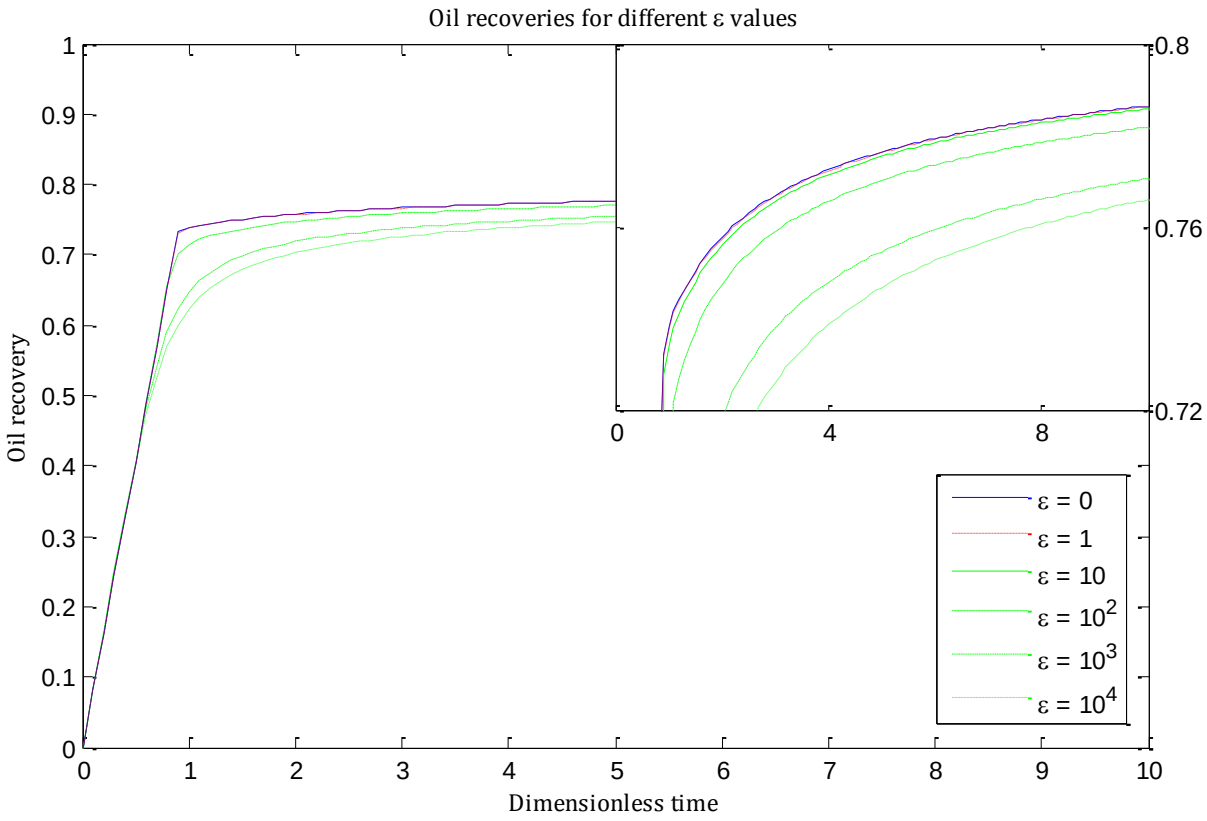

Figure 27: Plot showing a comparison of oil recoveries for different epsilon values. See Appendix C for other input parameters.

5 Modelling using low salinity effects

While the basic forms of the Buckley-Leverett model are more applicable when considering secondary recovery processes, there exist a number of extensions to the model that aim to implement the effect of EOR processes. Common examples of this are chemical processes such as polymer injection and/or surfactants. In the case of polymer injection the aim would be to effect the viscosity of the water flood to better achieve mobility control, as discussed in Chapter 3.1. A surfactant flood will aim to effect interfacial properties and in effect change residual oil and thus increase the oil recovery. In both these cases there exist established methods to model this behaviour as presented by Green and Willhite [4].

Another EOR process that is currently of interest in industry is referred to as low salinity (or lowsal) water injection. It has been reported that the salinity and composition of brine can increase oil recovery from water floods in sandstone reservoirs. In a paper by Omekeh et. al. [1] a method of modelling lowsal effects is presented. The proposed model is based on the one dimensional BL model, but has been modified to include low salinity effects using a multiple ion exchange (MIE) mechanism.

The suggested model is an example of how the BL model can be used to describe more complex behaviour involving chemical interaction and rock wettability. Throughout the remainder of this thesis this model will be investigated in some detail, by deriving the model and presenting results from numerical simulations. These numerical simulations have been run using the same MATLAB programme as that used in the paper. For the details, which are outside the scope of this text, we refer to [1].

5.1 The model

In summary, the model described in [1] is divided into three main parts. The first part describes a sandstone reservoir (represented by a sandstone core plug) which contains a certain amount of clay, and is linked to the ion exchange reactions. Secondly, the MIE process is included,

involving the Ca^{2+}, Mg^{2+} and Na^{+} ions. The last part implements a coupling between divalent ions that are released from the rock surface, and a change in water-oil relative permeability curves that will lead to an increased oil recovery.

5.1.1 Multiple ion exchange

In general we distinguish between chemical activity a and concentration C:

$$a = \gamma C \tag{5.1}$$

where γ is the activity coefficient, which can be determined using the extended Debuye-Hückel equation (see [1] for more details):

$$\log_{10}(\gamma_i) = \frac{-AZ_i^2\sqrt{I_0}}{1 + a_i^0 B\sqrt{I_0}} + bI_0 \tag{5.2}$$

$$I_0 = \frac{1}{2}\sum_i C_i Z_i^2 \tag{5.3}$$

Here A and B are given temperature dependent functions, Z_i refer to ionic charge, a_i^0 are given constants, b is an extended term parameter and I_0 refers to the ionic strength.

When discussing cation exchange the H^+ ion will typically have a stronger displacing power than Ca^{2+}, Mg^{2+} and Na^{+} ions, however its concentration in oil reservoirs is considered to be low compared to that of the other ions. Thus, the amount of H^+ ions on the clay surface is expected to be negligible, and is therefore ignored in the model. Now the Gapon model is used to model cation exchange as

$$\frac{1}{2}Ca^{2+} + Na\text{–}X \rightleftharpoons Ca_{\frac{1}{2}}\text{–}X + Na^{+} \tag{5.4}$$

$$\frac{1}{2}Mg^{2+} + Na\text{–}X \rightleftharpoons Mg_{\frac{1}{2}}\text{–}X + Na^{+} \tag{5.5}$$

By using a set of constant selectivity factors K_{cana} and K_{mgna} with the Gapon model the authors derive a set of functions that describe the amount of Ca^{2+}, Mg^{2+} and Na^{+} ions attached to the clay surface:

$$\beta_{na}(C_{na}, C_{ca}, C_{mg}) = \frac{\gamma_{na} C_{na} CEC}{2K_{cana}\sqrt{\gamma_{ca} C_{ca}} + 2K_{mgna}\sqrt{\gamma_{mg} C_{mg}} + \gamma_{na} C_{na}} \tag{5.6}$$

$$\beta_{ca}(C_{na}, C_{ca}, C_{mg}) = \frac{K_{cana}\sqrt{\gamma_{ca} C_{ca}} CEC}{2K_{cana}\sqrt{\gamma_{ca} C_{ca}} + 2K_{mgna}\sqrt{\gamma_{mg} C_{mg}} + \gamma_{na} C_{na}} \tag{5.7}$$

$$\beta_{mg}(C_{na}, C_{ca}, C_{mg}) = \frac{K_{mgna}\sqrt{\gamma_{mg} C_{mg}} CEC}{2K_{cana}\sqrt{\gamma_{ca} C_{ca}} + 2K_{mgna}\sqrt{\gamma_{mg} C_{mg}} + \gamma_{na} C_{na}} \tag{5.8}$$

Here the CEC parameter is defined as the cation exchange capacity (given in equivalent/Kg units), and relates the three β-functions.

5.1.2 Changing wettability conditions

As discussed in section 3.2.1, the relative permeability functions will be related to the wetting conditions present in a reservoir. Since this version of the model ignores capillary pressure it is convenient to assume that the wettability is represented by the relative permeability functions only. We will also assume that the MIE process is able to effect wettability conditions, changing initial wetting conditions to more favourable wetting condition. The initial conditions are referred to as high salinity conditions while the effected state is considered as a low salinity condition. In the case of low salinity conditions we assume that there is complete desorption of Ca^{2+} and Mg^{2+} ions from the clay surface.

For this purpose, two sets of relative permeability curves are used. These curves are defined using the Corey relative permeability functions as discussed in section 3.2.2, and are given the following notation

$$k_{rw}^{HS}(S), \qquad k_{ro}^{HS}(S), \qquad S_{wi}^{HS} \leq S \leq 1 - S_{or}^{HS} \tag{5.9}$$

$$k_{rw}^{LS}(S), \qquad k_{ro}^{LS}(S), \qquad S_{wi}^{LS} \leq S \leq 1 - S_{or}^{LS} \tag{5.10}$$

where upper case *HS* and *LS* indicate high salinity and low salinity conditions (see Figure 28).

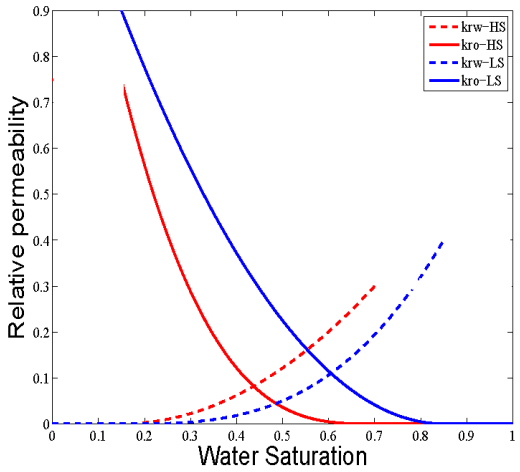

Figure 28: Plot showing relative permeability curves corresponding to high salinity conditions (HS) and low salinity conditions (LS). This figure is taken from Figure 2 in [1].

To implement a change from one wetting condition to the other, we start by defining β_{ca0} and β_{mg0}. These parameters represent the initial amount of ions calcium and magnesium that are bound to the rock surface. Using these parameters we define a quantity

$$m(\beta_{ca}, \beta_{mg}) := \max(\beta_{ca0} - \beta_{ca}, 0) + \max(\beta_{mg0} - \beta_{mg}, 0) \tag{5.11}$$

and the *H*-function

$$H(\beta_{ca}, \beta_{mg}) := \frac{1}{1 + rm(\beta_{ca}, \beta_{mg})} \tag{5.12}$$

Using the *H*-function an interpolation from the high salinity condition to the low salinity condition is proposed, and is expressed as

$$k(S, \beta_{ca}, \beta_{mg}) = H(\beta_{ca}, \beta_{mg}) k_{rw}^{HS}(S) + \left[1 - H(\beta_{ca}, \beta_{mg})\right] k_{ro}^{LS}(S) \tag{5.13}$$

5.1.3 The coupled model

Compared with the simpler BL models presented earlier, this model also needs to account for convective and diffusive forces associated with the oil and brine. As a first step we consider the differential equations using total concentrations $\rho_o, \rho_l, \rho_{ca}, \rho_{ca}, \rho_{so}, \rho_{cl}, \rho_{mg}$ (mol per litre core):

$$\partial_t \rho_o + \nabla \cdot (\rho_o \mathbf{v}_o) = 0$$

$$\partial_t \rho_l + \nabla \cdot (\rho_l \mathbf{v}_l) = 0$$

$$\partial_t \rho_{na} + \partial_t (M_c \beta_{na}) + \nabla \cdot (\rho_{na} \mathbf{v}_g) = 0$$

$$\partial_t \rho_{cl} + \nabla \cdot (\rho_{cl} \mathbf{v}_g) = 0 \tag{5.14}$$

$$\partial_t \rho_{ca} + \partial_t (M_c \beta_{ca}) + \nabla \cdot (\rho_{ca} \mathbf{v}_g) = 0$$

$$\partial_t \rho_{so} + \nabla \cdot (\rho_{so} \mathbf{v}_g) = 0$$

$$\partial_t \rho_{mg} + \partial_t (M_c \beta_{mg}) + \nabla \cdot (\rho_{ca} \mathbf{v}_g) = 0$$

where $\mathbf{v}_o$, $\mathbf{v}_l$ and $\mathbf{v}_g$ are oil, water and species "fluid" velocities respectively, while M_c represents the mass of clay present in the reservoir.

Similar to subsequent derivations of the BL model in chapters 2 and 3, the low salinity model assumes that there are only two phases flowing, which implies that $S_o + S = 1$. However, the low salinity model also introduces porous concentrations that are associated to the two phases, where the concentration of brine is defined by the concentration of water and the different ion species. For the oil phase, the porous concentration C_o is related to oil density and expressed as

$$\rho_o = \varphi S C_o \tag{5.15}$$

Similarly, the porous concentrations present in the brine are given by

$$\rho_i = \varphi S C_i, \ i = l, na, cl, ca, so, mg \tag{5.16}$$

The authors argue that interstitial velocities $\mathbf{v}_o$, $\mathbf{v}_l$ and $\mathbf{v}_g$ differ from velocities $\mathbf{V}_o$, $\mathbf{V}_l$ and $\mathbf{V}_g$, and use the Dupuit-Forchheimer relation to express this relationship:

$$\mathbf{V}_o = \varphi S_o \boldsymbol{v}_o,\ \mathbf{V}_l = \varphi S \boldsymbol{v}_l,\ \mathbf{V}_g = \varphi S \mathbf{v}_l \tag{5.17}$$

To close the system these velocities need to be determined. In order to do this the total concentration of ions C_g and brine concentration C need to be defined:

$$C_g = C_{na} + C_{cl} + C_{ca} + C_{mg} + C_{so},\ C = C_g + C_l \tag{5.18}$$

Using C we then define an associated velocity $\mathbf{V}$ giving

$$C\mathbf{V} := C_g \mathbf{V}_g + C_l \mathbf{V}_l \tag{5.19}$$

Now we are able to rewrite the model in terms of the diffusivity velocity $\mathbf{U}_g$, expressed as

$$\mathbf{U}_g = \mathbf{V}_g - \mathbf{V} \tag{5.20}$$

Rewriting the model as shown in (5.14) we obtain

$$\partial_t(\varphi S_o C_o) + \nabla \cdot (C_o \mathbf{V}_o) = 0$$

$$\partial_t(\varphi S C_l) + \nabla \cdot (C_l \mathbf{V}_l) = 0$$

$$\partial_t(\varphi S C_{na}) + \partial_t(M_c \beta_{na}) + \nabla \cdot \left(C_{na} \mathbf{U}_g\right) = -\nabla \cdot (C_{na} \mathbf{V})$$

$$\partial_t(\varphi S C_{cl}) + \nabla \cdot \left(C_{cl} \mathbf{U}_g\right) = -\nabla \cdot (C_{cl} \mathbf{V}) \tag{5.21}$$

$$\partial_t(\varphi S C_{ca}) + \partial_t(M_c \beta_{ca}) + \nabla \cdot \left(C_{ca} \mathbf{U}_g\right) = -\nabla \cdot (C_{ca} \mathbf{V})$$

$$\partial_t(\varphi S C_{so}) + \nabla \cdot \left(C_{so} \mathbf{U}_g\right) = -\nabla \cdot (C_{so} \mathbf{V})$$

$$\partial_t\left(\varphi S C_{mg}\right) + \partial_t\left(M_c \beta_{mg}\right) + \nabla \cdot \left(C_{mg} \mathbf{U}_g\right) = -\nabla \cdot (C_{mg} \mathbf{V})$$

The velocities $\mathbf{V}$ and $\mathbf{V_o}$ can now be expressed using phase velocities (Darcy velocities) as described in Chapter 2.1:

$$\mathbf{V} = \lambda_w(\nabla p_w - \rho_w g \nabla d) \tag{5.22}$$

$$\mathbf{V_o} = \lambda_o(\nabla p_o - \rho_o g \nabla d) \tag{5.23}$$

while the diffusivity velocity $\mathbf{U_g}$ is expressed using Flick's law

$$C_i \mathbf{U_g} = -D\nabla C_i, \ i = na, cl, ca, so, mg \tag{5.24}$$

Here *D* represents the diffusion coefficient and the same for all species; Na^+, Cl^-, Ca^{2+}, Mg^{2+} and SO_4^{2-}. The authors also mention that there are concentration limits when using the relationship, but this model is reasonable to use since the ion concentrations are relatively small.

Furthermore, the coefficient *D* is defined from two contributions; diffusion and mechanical/advective, and is determined using a formulation of Sahimi using the Pécelet number (see page 10 [1] for more details).

Using *D* in (5.21) we get

$$\partial_t(\varphi S_o C_o) + \nabla \cdot (C_o \mathbf{V}_o) = 0$$

$$\partial_t(\varphi S C_l) + \nabla \cdot (C_l \mathbf{V}_l) = 0$$

$$\partial_t(\varphi S C_{na}) + \partial_t(M_c \beta_{na}) - \nabla \cdot (D\nabla C_{na}) = -\nabla \cdot (C_{na}\mathbf{V})$$

$$\partial_t(\varphi S C_{cl}) - \nabla \cdot (D\nabla C_{cl}) = -\nabla \cdot (C_{cl}\mathbf{V}) \tag{5.25}$$

$$\partial_t(\varphi S C_{ca}) - \partial_t(M_c \beta_{ca}) + \nabla \cdot (D\nabla C_{ca}) = -\nabla \cdot (C_{ca}\mathbf{V})$$

$$\partial_t(\varphi S C_{so}) - \nabla \cdot (D\nabla C_{so}) = -\nabla \cdot (C_{so}\mathbf{V})$$

$$\partial_t\big(\varphi S C_{mg}\big) + \partial_t\big(M_c \beta_{mg}\big) - \nabla \cdot \big(D\nabla C_{mg}\big) = -\nabla \cdot (C_{mg}\mathbf{V})$$

Summing the equations corresponding to the ion concentrations C_i we obtain an expression in terms of C_g:

$$\partial_t(\varphi S C_g) + \partial_t\left(M_c\left[\beta_{na} + \beta_{ca} + \beta_{mg}\right]\right) + \nabla \cdot \left(D \nabla C_g\right) = -\nabla \cdot (C_g \mathbf{V}) \tag{5.26}$$

Using equations (5.18),(5.19) and (5.20) we can express $C_l \mathbf{V}_l = C_l \mathbf{V} - C_g \mathbf{U}_g$ and using the second equation in (5.21) we get

$$\partial_t(\varphi S C) + \nabla \cdot (C_l \mathbf{V}) = -\nabla \cdot (C_g \mathbf{U}_g) \tag{5.27}$$

Finally we add (5.26) and (5.27), with $C = C_g + C_l$, to get

$$\partial_t(\varphi S C) + \partial_t\left(M_c\left[\beta_{na} + \beta_{ca} + \beta_{mg}\right]\right) + \nabla \cdot (C \mathbf{V}) = 0 \tag{5.28}$$

Using this equation in (5.25) leaves us with the following model

$$\partial_t(\varphi S_o C_o) + \nabla \cdot (C_o \mathbf{V}_o) = 0$$

$$\partial_t(\varphi S C) + \partial_t\left(M_c\left[\beta_{na} + \beta_{ca} + \beta_{mg}\right]\right) + \nabla \cdot (C \mathbf{V}) = 0$$

$$\partial_t(\varphi S C_{na}) + \partial_t(M_c \beta_{na}) + \nabla \cdot (C_{na} \mathbf{V}) = \nabla \cdot (D \nabla C_{na})$$

$$\partial_t(\varphi S C_{cl}) + \nabla \cdot (C_{cl} \mathbf{V}) = \nabla \cdot (D \nabla C_{cl}) \tag{5.29}$$

$$\partial_t(\varphi S C_{ca}) + \partial_t(M_c \beta_{ca}) + \nabla \cdot (C_{ca} \mathbf{V}) = \nabla \cdot (D \nabla C_{ca})$$

$$\partial_t(\varphi S C_{so}) + \nabla \cdot (C_{so} \mathbf{V}) = \nabla \cdot (D \nabla C_{so})$$

$$\partial_t\left(\varphi S C_{mg}\right) + \partial_t\left(M_c \beta_{mg}\right) + \nabla \cdot (C_{mg} \mathbf{V}) = \nabla \cdot \left(D \nabla C_{mg}\right)$$

5.1.4 Simplifying the model

Similar to other forms of the BL equations discussed previously, a set of simplifying assumptions are used:

- One dimensional flow through a horizontal reservoir
- A set of constant reservoir and fluid parameters; φ, k, μ_o, μ_w.
- Capillary pressure is set to zero.

- Incompressible fluids are assumed which implies that oil and water component densities C and C_o are constant.
- It is argued that the effect related to water-rock chemistry in equation two of (5.29) can be neglected since the concentration of water C is much larger than the concentration of ion components involved in the chemical reactions.

Using these assumptions with (5.29) result in the following expressions

$$\partial_t(\varphi S_o) + \partial_x(V_o) = 0$$

$$\partial_t(\varphi S) + \partial_x(V) = 0$$

$$\partial_t(\varphi S C_{na}) + \partial_t(M_c \beta_{na}) + \partial_x(C_{na} V) = \partial_x(D \partial_x C_{na})$$

$$\partial_t(\varphi S C_{cl}) + \partial_x(C_{cl} V) = \partial_x(D \partial_x C_{cl}) \tag{5.30}$$

$$\partial_t(\varphi S C_{ca}) + \partial_t(M_c \beta_{ca}) + \partial_x(C_{ca} V) = \partial_x(D \partial_x C_{ca})$$

$$\partial_t(\varphi S C_{so}) + \partial_x(C_{so} V) = \partial_x(D \partial_x C_{so})$$

$$\partial_t\big(\varphi S C_{mg}\big) + \partial_t\big(M_c \beta_{mg}\big) + \partial_x(C_{mg} V) = \partial_x\big(D \partial_x C_{mg}\big)$$

where $D = D(\varphi, S)$.

Using the same approach as in Chapter 2.2 an expression for total velocity v_T can be found

$$v_T = V_o + V = \lambda \partial_x p \tag{5.31}$$

where v_T will remain constant.

A set of simplified fractional flow functions are defined for water and oil:

$$f\big(S, \beta_{ca}, \beta_{mg}\big) = \frac{\lambda_w(S, \beta_{ca}, \beta_{mg})}{\lambda_w\big(S, \beta_{ca}, \beta_{mg}\big) + \lambda_o(S, \beta_{ca}, \beta_{mg})} \tag{5.32}$$

$$f_o(S,\beta_{ca},\beta_{mg}) = \frac{\lambda_o(S,\beta_{ca},\beta_{mg})}{\lambda_w(S,\beta_{ca},\beta_{mg}) + \lambda_o(S,\beta_{ca},\beta_{mg})} \tag{5.33}$$

where $f_o(S,\beta_{ca},\beta_{mg}) = 1 - f(S,\beta_{ca},\beta_{mg})$.

The water fractional flow function seen here is similar to that used in Chapter 2.2, but opposed to that version, this function also relies on β_{ca} and β_{mg}. These parameters are used in the H-function, to interpolate between two relative permeability functions which represent different wetting conditions.

In view of (5.22), (5.23), (5.31), (5.32) and (5.33) a model is obtained of the form

$$\begin{gathered}
\partial_t(\varphi S) + v_T \partial_x f = 0 \\
\partial_t(\varphi S C_{na} + M_c \beta_{na}) + v_T \partial_x(C_{na} f) = \partial_x(D \partial_x C_{na}) \\
\partial_t(\varphi S C_{cl}) + v_T \partial_x(C_{cl} f) = \partial_x(D \partial_x C_{cl}) \\
\partial_t(\varphi S C_{ca} + M_c \beta_{ca}) + v_T \partial_x(C_{ca} f) = \partial_x(D \partial_x C_{ca}) \\
\partial_t(\varphi S C_{so}) + v_T \partial_x(C_{so} f) = \partial_x(D \partial_x C_{so}) \\
\partial_t(\varphi S C_{mg} + M_c \beta_{mg}) + v_T \partial_x(C_{mg} f) = \partial_x(D \partial_x C_{mg})
\end{gathered} \tag{5.34}$$

where $f = f_o(S,\beta_{ca},\beta_{mg})$ and $D = D(\varphi, S)$.

Using previously introduced dimensionless variables x_D and t_D along with a new set of dimensionless coefficients

$$D_{mD} = \frac{D_m}{D_{m,ref}}, \qquad \mu = \frac{\mu}{\mu_{ref}} \tag{5.35}$$

and the variables

$$c_1 = \varphi S C_{na}, c_2 = \varphi S C_{cl}, c_3 = \varphi S C_{ca}, c_4 = \varphi S C_{so}, c_5 = \varphi S C_{mg} \tag{5.36}$$

$$B_1 = M_c\beta_{na}, B_3 = M_c\beta_{ca}, B_5 = M_c\beta_{mg} \tag{5.37}$$

the model (5.34) can be simplified to (skipping the dimensionless indicator; subscript *D*)

$$\partial_t(\varphi S) + \partial_x(\varphi f) = 0$$

$$\partial_t(c_1 + B_1) + \partial_x(C_{na}\varphi f) = \delta\partial_x(D_m\varphi^p S^q \partial_x C_{na})$$

$$\partial_t(c_2) + v_T\partial_x(C_{cl}\varphi f) = \delta\partial_x(D_m\varphi^p S^q \partial_x C_{cl}) \tag{5.38}$$

$$\partial_t(c_3 + B_3) + v_T\partial_x(C_{ca}\varphi f) = \delta\partial_x(D_m\varphi^p S^q \partial_x C_{ca})$$

$$\partial_t(c_4) + v_T\partial_x(C_{so}\varphi f) = \delta\partial_x(D_m\varphi^p S^q \partial_x C_{so})$$

$$\partial_t(c_5 + B_5) + v_T\partial_x(C_{mg}\varphi f) = \delta\partial_x\left(D_m\varphi^p S^q \partial_x C_{mg}\right)$$

Here δ represents a characteristic dimensionless number expressed as

$$\delta = \frac{\varphi D_{m,ref}}{L v_T} \tag{5.39}$$

Note that $D = D_m\varphi^p S^q$, is taken from the formulation by Sahimi mentioned earlier.

5.1.5 Boundary conditions and initial conditions

At the inlet and outlet of the reservoir, the following Dirichlet boundary conditions are used

$$S(0,t) = S(1,t) = 1.0 \tag{5.40}$$

$$C_i(0,t) = C_i(1,t) = C_i^*, \qquad i = na, cl, ca, so, mg \tag{5.41}$$

where C_i^* represents a given species concentration in the brine. Note that the outlet conditions are applied using extrapolation for S and C_i values.

The initial conditions state that the reservoir rock is filled with oil, and an initial water saturation (S_{wi}) of 15%. Therefore we have

$$S(x,0) = S_{wi} = 0.15, \qquad 0 \leq x \leq 1 \tag{5.42}$$

$$C_i(x,0) = C_{i0}, \qquad 0 \leq x \leq 1, \qquad i = na, cl, ca, so, mg \tag{5.43}$$

where C_{i0} are the initial concentration of the various species in the brine.

5.2 Solution procedure

The numerical solution procedure used for the low salinity model in part uses a scheme similar to that described in section 2.3.2. This discretization is based on a relaxation scheme, but details of this procedure are outside the scope of this text, and instead refer to section 5.1 of [1]. Note also that the contribution from MIE to the model adds a level of complexity to the solution procedure in terms of a nonlinear system of equations.

5.3 Effect of brine composition on model behaviour

As stated earlier, the reservoir (core plug) is initially filled with oil and a certain amount of formation water. This water will initially be at equilibrium with the ions on the clay surface. This state has been called a high salinity condition, representing an initial wetting state of the reservoir. When a water flood containing brine different from the formation water is introduced to this system, concentration fronts are established (see Figure 29). Concentration differences will disrupt the state of equilibrium giving rise to chemical reactions at and behind the front. These reactions described by the MIE will effect the wettability, giving rise to more favourable wetting conditions and mobilization of additional oil. The aim of the numerical experiments presented here, will be to show the effect brine compositions has on model behaviour and how this effects oil recovery.

The grid is divided into 40 cells in the *x* domain. The authors [1] compare simulation results using 40 and 120 grid cells for a number of time values, and conclude that results using 40 grid cells are satisfactory. However, using a less refined grid may have an impact on oil recovery, as discussed in section 2.3.3. On the other hand, increasing the number of grid cells in the proposed

model, is expected to have a much greater impact on simulation run-time compared to this effect on the simpler BL model presented earlier. This is presumed to also have been factored in when the authors defend using the less refined grid.

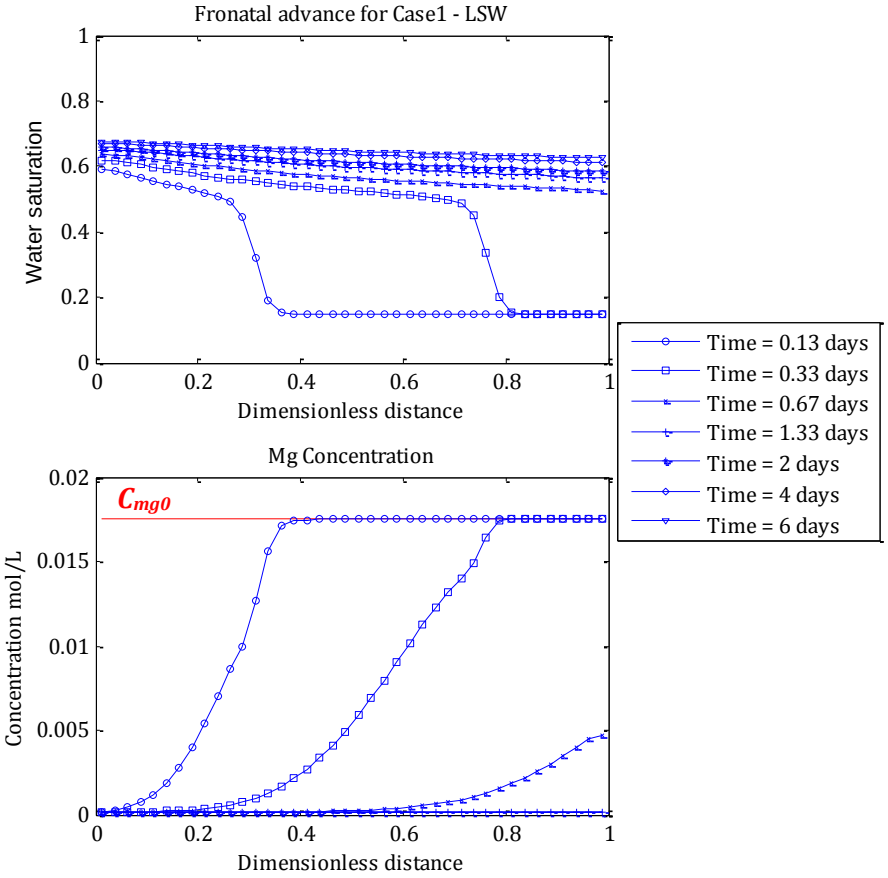

Figure 29: Saturation fronts and Mg^{2+} concentration fronts at different time values, using LSW as the invading brine.

As a final point, it is important to note that the high and low salinity conditions represent the recovery boundaries. Using the relative permeability functions for these salinity conditions we find oil recoveries as shown in Figure 30.

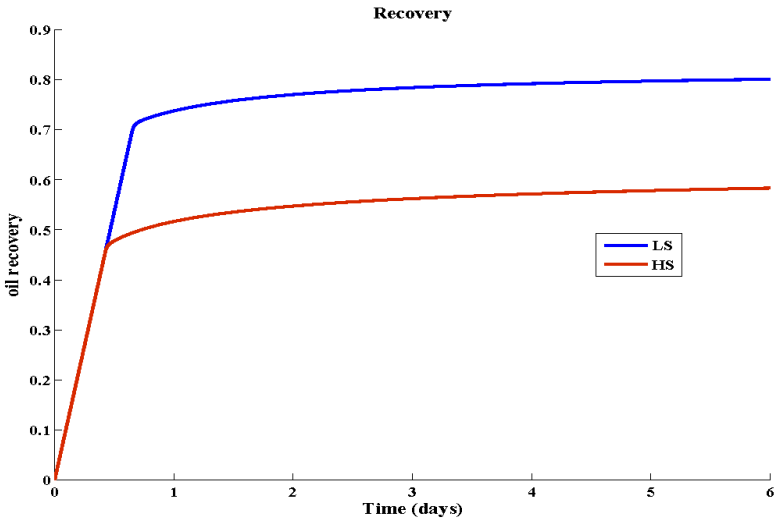

Figure 30: Plot showing oil recoveries for high salinity (HS) and low salinity(LS) conditions. This figure is taken from Figure 4 in [1].

5.3.1 Simulation results

The sandstone core used as a basis for the simulations is composed of clay and other minerals, and is assumed to be chemically non-reactive for modelling purposes. The mass of clay and CEC present in the core are supplied in Appendix D.

The core is initially saturated with oil and an initial water saturation of 15 %. This initial water, or rather formation water, contains concentrations as stated for FW. The core is subsequently flooded with invading brines with $v_T = 0.01$ m/day and $t = 6$ days. These floods are run until insignificant amounts of oil are produced relative to PVs of brine injected.

Input parameters used to compute the different solutions are given in Appendix D and a set of four brine compositions are used; LSW, LSW1, LSW2 and LSW3 (see Table 2 in Appendix D). These brine compositions have been modified using ion concentrations, and corresponding ion strength. All other input parameters remain fixed.

The initial flood LSW is based on FW which has been diluted 100 times, while LSW1 is similarly diluted 10 times. The LSW2 flood uses LSW1 as a basis, adjusting the concentration of magnesium. In LSW3 the concentrations from LSW1 are also used, but in this case both divalent ions (magnesium and calcium) are modified. An example of ion concentrations used in an

invading brine is given in Figure 31, and shows Mg^{2+}, Ca^{2+}, Na^{+} and Cl^{-} composition used for the LSW brine.

In Figure 32 we can see β-functions for Ca^{2+}, Mg^{2+} and Na^{+}. These functions represent the amount of ions present on the clay surface in the case of LSW invading brine, where the red line indicates the initial state corresponding to a state of equilibrium. The blue lines show a disruption of this state of equilibrium, and eventually a new state of equilibrium being achieved, after a certain amount of time.

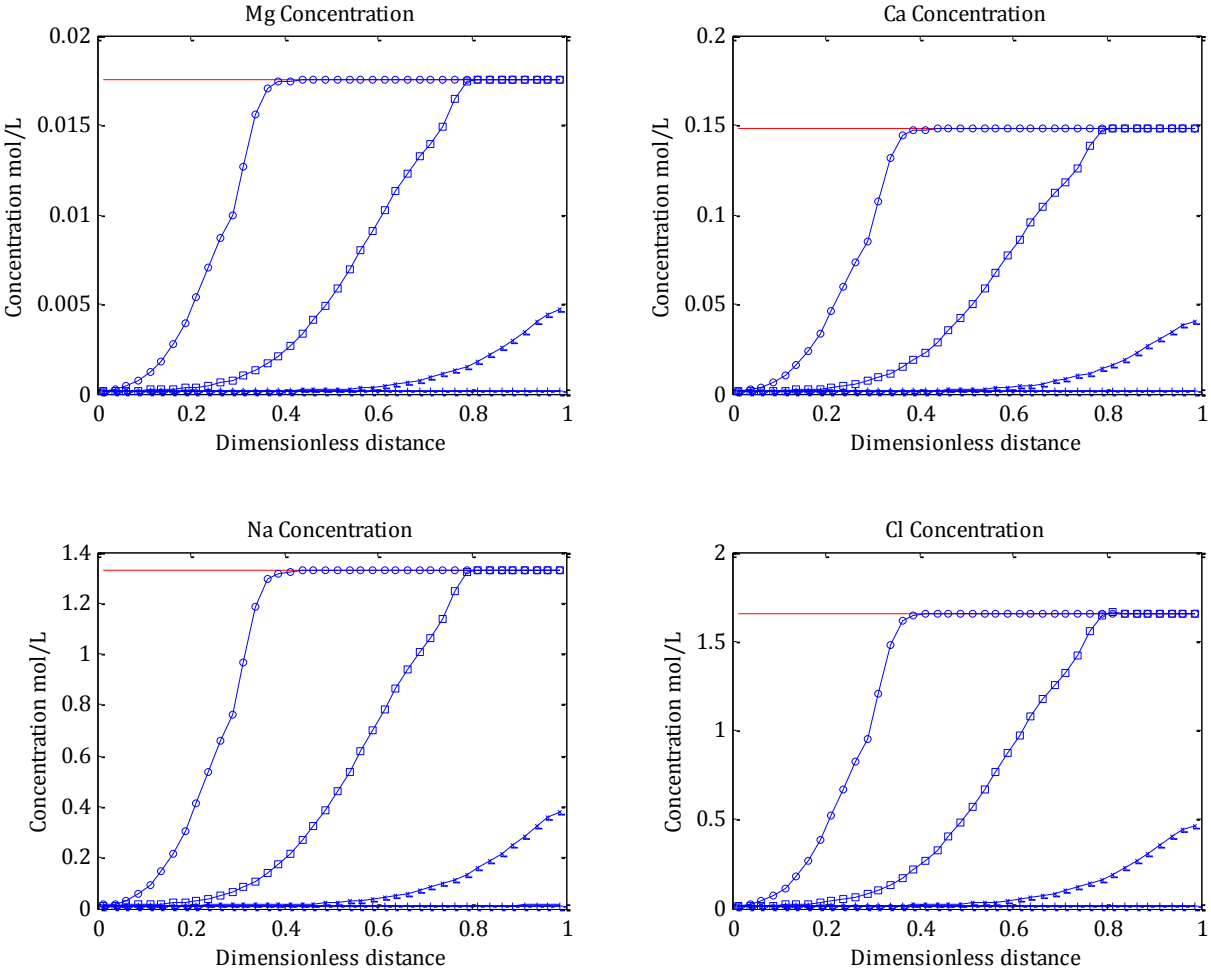

Figure 31: Ion concentrations for invading brine using LSW composition. Concentrations are shown along the length of the core, for a series of time values and ending at; $t = 6$ days.

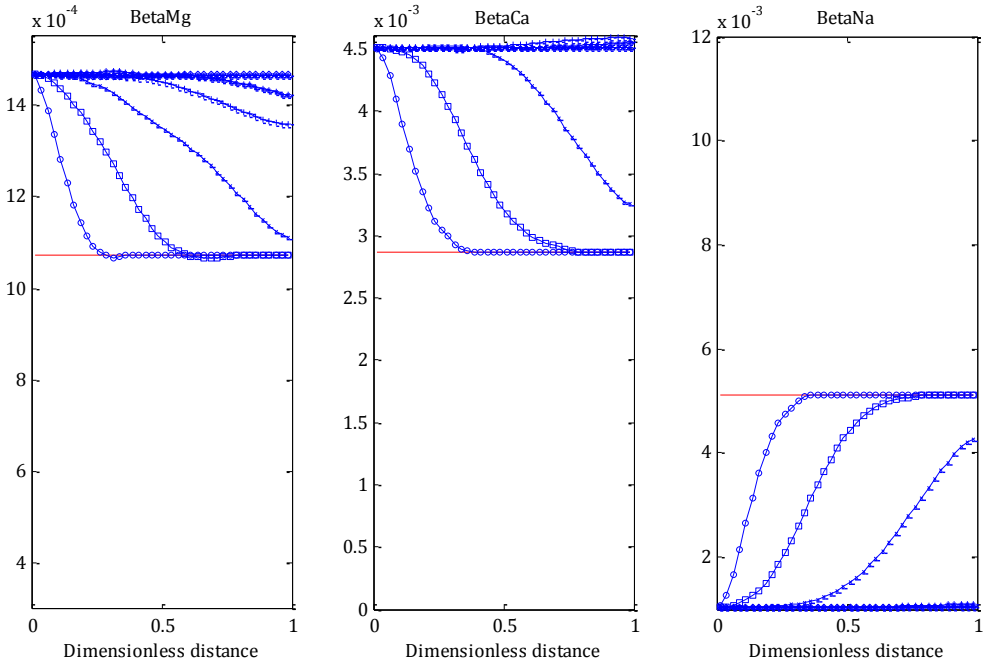

Figure 32: Plots showing the β-function along the core at different time values, using LSW brine. Note that there is no desorption of divalent ions, only adsorption. Left: β_{mg}. Middle: β_{ca}. Right: β_{na}.

In order to see changes in wetting state one would expect a certain amount of desorption of divalent ions. However, in this case we see no effects of this desorption, we only see changes in β-values that can be related to an adsorption of ions. This corresponds to the constant values of *H* seen in Figure 33, and comparing the *H*-funtion value of 1 with (5.13) we note that in this case the model only uses the high salinity relative permeability function to compute solutions.

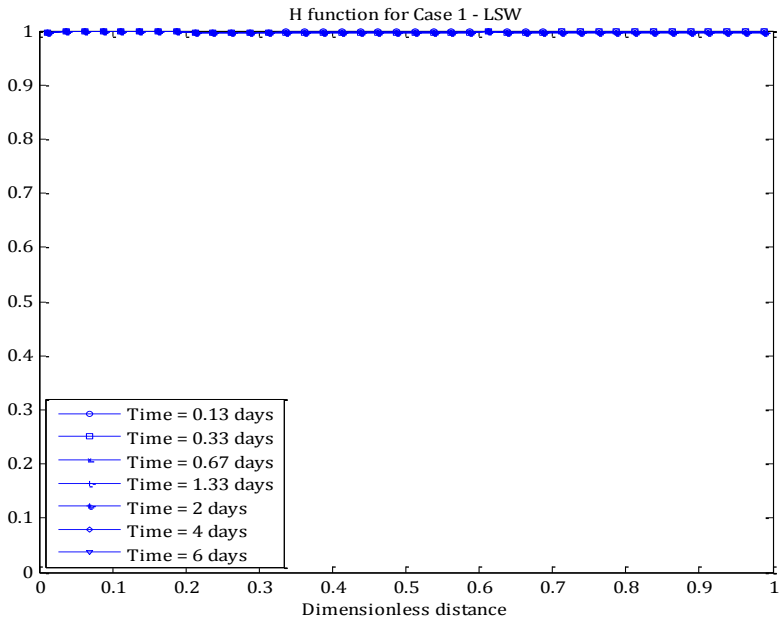

Figure 33: The H-function corresponding to β-functions for LSW invading brine. In this case there is no response since there is no desorption of divalent ions.

Considering the β-functions for LSW3 in Figure 34, we notice decreasing β-values for magnesium and calcium, whereas these values were increasing for the LSW case (Figure 32). This decrease in value can be tied to desorption of divalent ions bonded to the clay surface, and corresponds to the effects seen on the *H*-function, as shown in Figure 35.

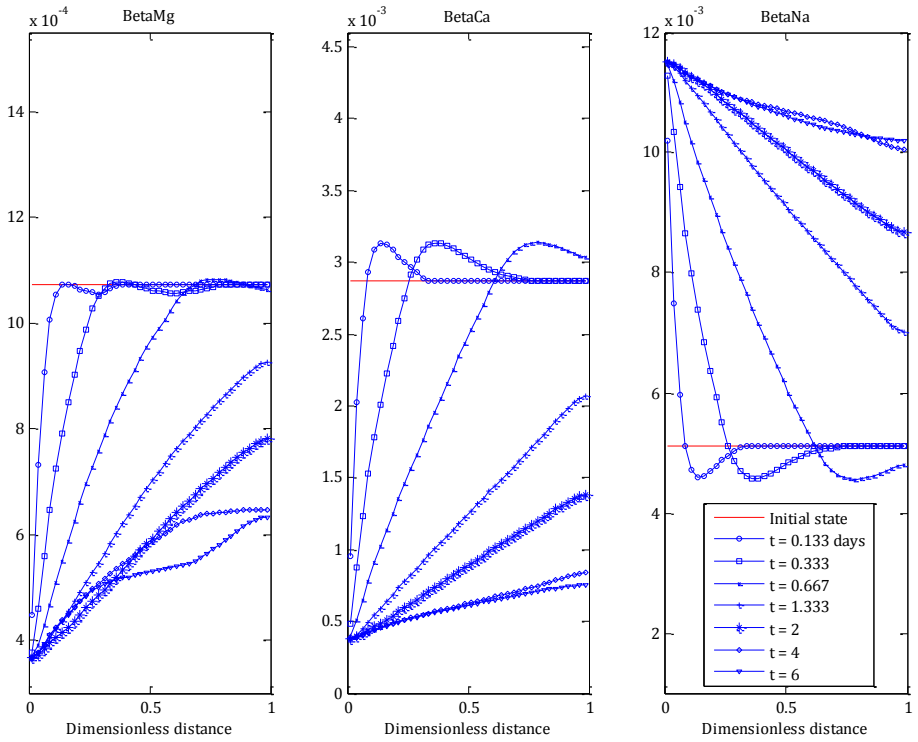

Figure 34: Plots showing the β-function along the core at different time values, using LSW brine. Note that there is desorption of divalent ions. Left: β_{mg}. Middle: β_{ca}. Right: β_{na}.

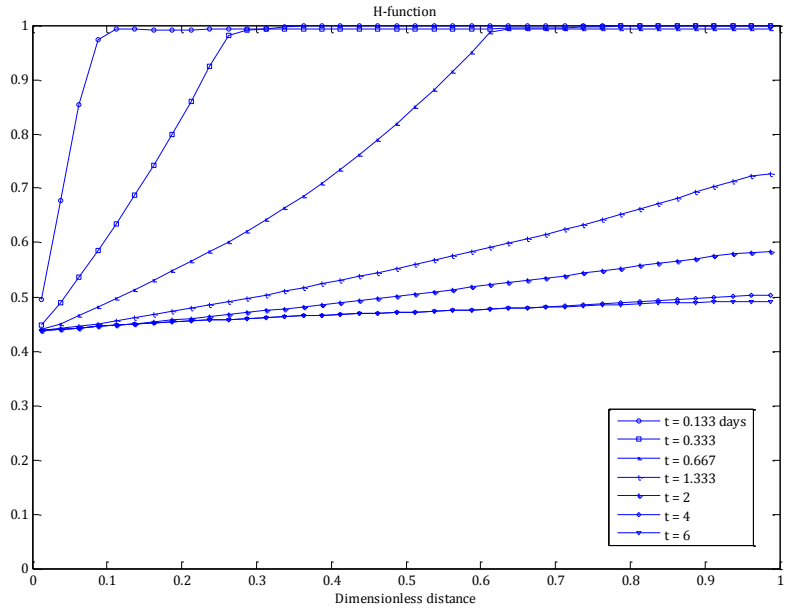

Figure 35: The H-function corresponding to β-functions for LSW3 invading brine. In this case there is a response due to the desorption of divalent ions.

Now we consider the oil recovery for all four solutions LSW, LSW1, LSW2 and LSW3 as shown in Figure 36. The blue curves indicate flooding using LSW1, LSW2 and LSW3, while the red curve indicates LSW. Comparing the recovery seen for LSW with the high salinity recovery (as seen in Figure 30) we see no change. Considering this in light of previous observations, this is expected since in Figure 37 we show flood front saturations for all the four cases, and observe model behaviour that ties to the mobilization of additional oil behind the front. This effect relates to the change in relative permeability functions that is being effected by the *H*-function. Considering Figure 35 we note that a reduction in *H* values gives rise to this behaviour, where the *H*-function acts as a weighting factor between the high and low salinity conditions.

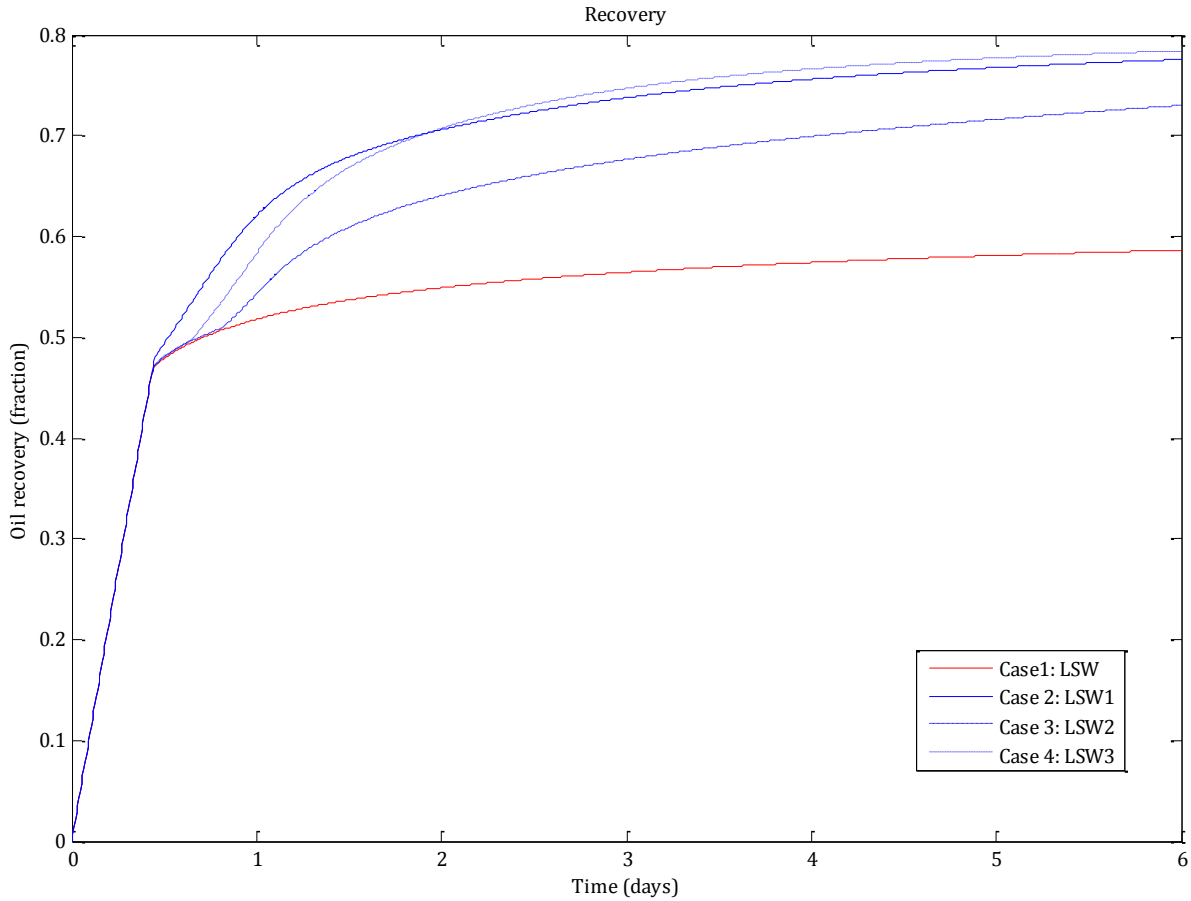

Figure 36: Oil recovery for invading brines with different salinity concentrations; LSW, LSW1, LSW2 and LSW3.

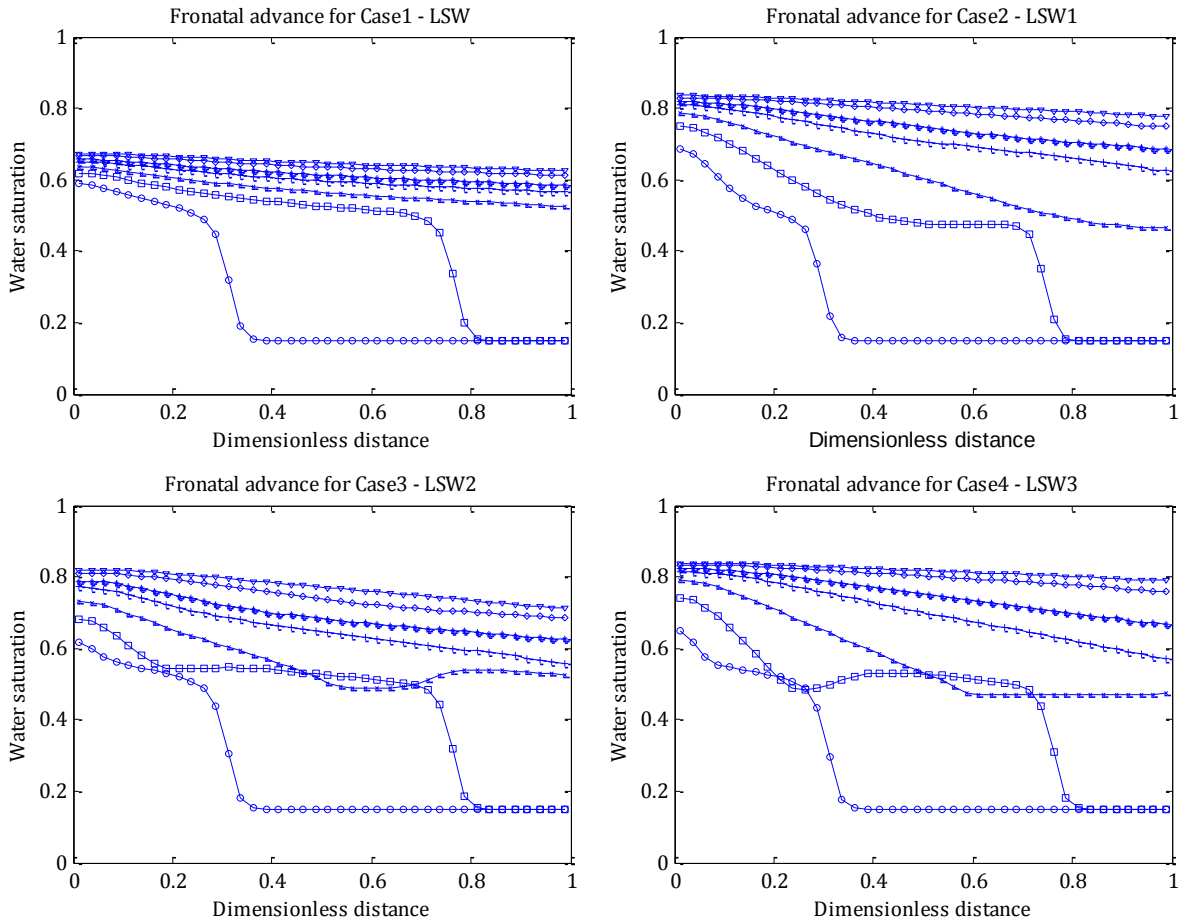

Figure 37: Plot showing the saturation S along the core for different time values, ending at t = 6 days. A mobilization of oil behind the front is seen for LSW1, LSW2 and LSW3. The additional mobilization of oil is due to changes in relative permeability tied to the H-function. Upper left: LSW. Upper right: LSW1. Lower left: LSW2. Lower right: LSW3.

Note that differences seen for the three brines showing positive low salinity effects (LSW1, LSW2 and LSW3), are results of varying degrees of ion dissolution. In the case of LSW1 we only see desorption of Ca^{2+}, while dissolution of both divalent ions occur in the other two cases. However the amount of desorption of calcium and magnesium seen for LSW2 is considerably lower than that seen for LSW1. These results differ slightly from the work done in [1], where the authors report that LSW2 shows only desorption of Ca^{2+}ions. This difference may be due to input errors, but does not seem to have a big impact on the oil recovery when comparing the Figure 36 in this work with Figure 8 in [1].

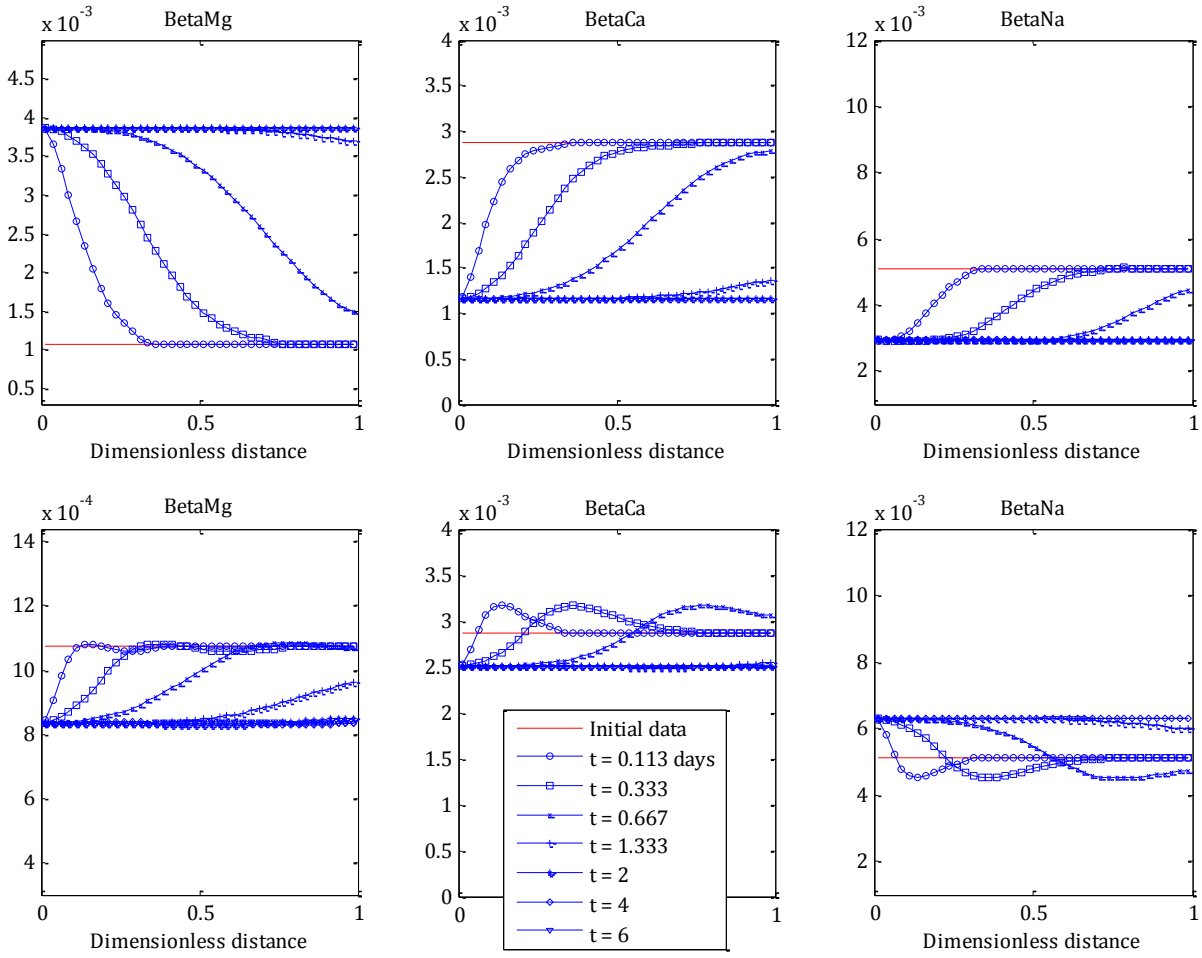

Figure 38: Plots showing the β-function along the core at different time values, for LSW1 and LSW2 brines. Note that there is desorption of divalent ions. Upper figures show results using LSW1 brine. Lower figures show results using LSW2 brine. Left: β_{mg}. Middle: β_{ca}. Right: β_{na}.

In [1] the authors present other interesting case comparisons. In two of these comparisons they let the concentration of the invading brine remain fixed and study the effect of changing formation water composition and behaviour tied to clay content and CEC. They also study the effects of different sea water being used as invading brine. In general, when designing a low salinity injection fluid, the most important factors are the clay content and the composition of the formation water that are present in the reservoir. Therefore, positive low salinity effects as described in this model are tied to a specific brine compositions which must be designed to react with a specific reservoir. For this purpose the modelling could be used to find the most efficient low salintity brine composition.

We should note that this model, and the results presented, build on the assumption that we are able to represent a reservoir using a set of realtive permeability functions. However, in a larger

model, having moved from core scale to reservoir scale this can be difficult. At production scale we would expect the reservoir to take on more heterogeneous behaviour, and it becomes more difficult to model appropriate wettability behaviour.

6 Conclusion

In the first part of this thesis we derived the classical one dimensional Buckley-Leverett Model, which is used to study immiscible displacement of two-phase fluid flow through a porous medium. This formulation was expanded to include effects due to gravity and capillary pressure. The gravity term was seen to be important when studying reservoirs with a given inclination, and showed significant effects on oil recovery. However, when studying capillary pressure we found that it was inversely proportional to the length of the reservoir, and therefore its significance was more important at a microscopic scale than at reservoir scale.

In the last part of the thesis we introduced the Low Salinity Model (see [1]), which leads to a further expansion of the Buckley-Leverett Model. There are indications that low salinity water injection could become a very important EOR method, and this is the motivation for this work. The Low Salinity model uses a transport-reaction model called multiple ion exchanges (MIE). This MIE process describes the interaction between ions bonded to clay in a reservoir matrix, and to the ions in displacing brine. Of particular importance are the β-functions which describe desorption/adsorption of ions bonded to the clay surface, and the H-function which effects the wettability change. From the simulation work performed, we note that there must be desorption of divalent ions to get an H-function response, and hence increase oil recovery.

In conclusion we note that studying a simplified model such as the Buckley-Leverett Model, gives a better understanding of certain physical processes that are important to understand when trying to optimise oil recovery. Comparing this type of model with more complex ones, such as a three dimensional Eclipse model, it is easier to isolate the effects of different physical properties.

In considering further work, it would be very interesting to compare results from the Low Salinity Model with results from experimental data. It would also be interesting to study the model with a focus on wettability at reservoir scale, and up-scaling the model.

References

[1] A. V. Omekeh, S. Evje og A. Friis, Modeling of Low Salinity Effects in Sandstone Oil Rocks, Institute for Scientific Computing and Information, 2004.

[2] H. Kleppe, Reservoir Simulation, University of Stavanger, 2010.

[3] S. E. Buckley og M. C. Leverett, Mechanism of Fluid Displacement in Sands, New York, 1941.

[4] D. W. Green og G. P. Willhite, Enhanced Oil Recovery, Richardson: Society of Petroleum Engineers, 1998.

[5] A. B. Zolotukhin og J.-R. Ursin, Introduction to Reservoir Engineering, Kristiansand: Norwegian Academic Press, 2000.

[6] R. H. Brooks og A. T. Corey, Hydraulic Properies of Porous Media, Colorado: Colorado State University, 1964.

[7] A. T. Corey, The Interrelation Between Gas and Oil Relative Permeabilities, 1954.

[8] W. Abdallah, J. S. Buckley, A. Carnegie, J. Edwards, E. Fordham, A. Graue, T. Habashy, N. Seleznev, C. Signer, H. Hussain, B. Montaron og M. Ziauddin, Fundamentals of Wettability, Oil Review, 2007.

[9] F. Lomeland, E. Ebeltoft og W. H. Thomas, A New Versatile Relative Permeability Correlation, Toronto, Canada: Reviewed paper at the International Symposium of the SCA, 21-25 August, 2005.

[10] C. R. Smith, G. W. Tracy og R. L. Farrar, Applied Reservoir Engineering Vol. 1, Tulsa, Oklahoma: OGCI and PetroSkills Publications, 1992.

[11] M. C. Leverett, Capillary Behavior in Porous Solids, Tulsa, 1940.

[12] F. Lomeland og E. Ebeltoft, A New Versatile Capillary Pressure, Abu Dhabi: International Symposium of the Society of Core Analysis, 2008.

[13] S. M. Skjaeveland, L. M. Siqveland, A. Kjosvik, W. L. Hammervold Thomas og G. A. Virnovsky, Capillary Pressure Correlation for Mixed-Wet Reservoirs, SPE, 2000.

Nomenclature

Parameter definitions followed by typical units used in the text.

A	Cross sectional area, m^2
f	Fractional flow, $volume\ fraction$
f'	Derivative of fractional flow, $volume\ fraction$
k	Absolute permeability, md
k_{rl}	Water relative permeability, $dimensionless$
k_{ro}	Oil relative permeability, $dimensionless$
L	Length, m
L, E, T	LET exponents
M	Viscosity ratio, $volume\ fraction$
n_w	Corey water exponent
n_w	Corey water exponent
n_o	Corey oil exponent
p	Pressure, bar
p_w	Water phase pressure, bar
p_o	Oil phase pressure, bar
P_c	Capillary pressure, bar
S	Saturation or water saturation, $volume\ fraction$
S_w	Water saturation, $volume\ fraction$
S_o	Water saturation, $volume\ fraction$
S_f	Flood front saturation, $volume\ fraction$
t	Time, $days$
t_D	Dimensionless time
T	Elapsed time, dimensionless
v	Darcy velocity, m/s
v_w	Water phase velocity, m/s

v_o	Oil phase velocity, m/s
x	Position (x-direction), m
x_D	Dimensionless position in x-direction
λ_w	Water phase mobility, md/cp
λ_o	Oil phase mobility, md/cp
λ_T	Total phase mobility, md/cp
μ	Viscosity, $fraction$
μ_w	Water viscosity, cp
μ_o	Oil viscosity, cp
σ_{ow}	Interfacial tension between oil and water, mN/m
θ	Contact angle, $degrees$
φ	Porosity, $fraction$

Appendix A: Input data for the simple Buckley-Leverett Model

Input data for Figure 3

- Number of grid cells used: $N = 500$
- Time used: $t = (0.1, 0.2, 0.4)$
- Corey exponents: $n_w = 2,\ n_o = 4$
- Viscosity ratio: $M = \mu_w/\mu_o = 0.5$

Input data for Figure 5

- Number of grid cells used: $N = 500$
- Time used: $t = 0.3$
- Corey exponents: $n_w = 2,\ n_o = 3$
- Viscosity ratio: $M = \mu_w/\mu_o = 0.5$

Input data for Figure 6

- Number of grid cells used: $N = (20, 100, 500)$
- Time used for saturation plots: $t = 0.5$
- Time used for recovery plot: $t = 10$
- Corey exponents: $n_w = 2,\ n_o = 3$
- Viscosity ratio: $M = \mu_w/\mu_o = 0.5$

Input data for Figure 7

- Corey exponents: $n_w = 2,\ n_o = 3$
- Viscosity ratio: $M = \mu_w/\mu_o = 0.5$

Input data for Figure 8

- Number of grid cells used: $N = 500$
- Time used for recovery plot: $t = 10$
- Corey exponents: $n_w = 2,\ n_o = 3$
- Viscosity ratios used: $M = \mu_w/\mu_o = (0.1, 0.5, 1.0)$

Input data for Figure 13

- Viscosity ratio: $M = \mu_w/\mu_o = 0.5$
- Initial water saturation: $S_{wi} = 0.2$
- Initial water saturation: $S_{wi} = 0.15$

Water-wet relative permeability, using Corey correlation

- Corey exponents: $n_w 3,\ n_o = 2$
- End-point oil relative permeability: $KRO = 0.95$
- End-point oil relative permeability: $KRW = 0.15$

Mixed-wet relative permeability, using Corey correlation

- Corey exponents: $n_w 3,\ n_o = 4$
- End-point oil relative permeability: $KRO = 0.65$
- End-point oil relative permeability: $KRW = 0.55$

Input data for Figure 14

- Number of grid cells used: $N = 200$
- Time used for saturation plots: $t = (0.1, 0.25, 0.5, 1, 5, 10)$
- Viscosity ratio: $M = \mu_w/\mu_o = 0.5$
- Initial water saturation: $S_{wi} = 0.2$
- Initial water saturation: $S_{wi} = 0.15$

Water-wet relative permeability, using Corey correlation

- Corey exponents: $n_w 3,\ n_o = 2$
- End-point oil relative permeability: $KRO = 0.95$
- End-point oil relative permeability: $KRW = 0.15$

Mixed-wet relative permeability, using Corey correlation

- Corey exponents: $n_w 3,\ n_o = 4$
- End-point oil relative permeability: $KRO = 0.65$

- End-point oil relative permeability: $KRW = 0.55$

Input data for Figure 15

- Number of grid cells used: $N = 200$
- Time used for recovery plot: $t = 10$
- Viscosity ratio: $M = \mu_w/\mu_o = 0.5$
- Initial water saturation: $S_{wi} = 0.2$
- Initial water saturation: $S_{wi} = 0.15$

Water-wet relative permeability, using Corey correlation

- Corey exponents: $n_w 3,\ n_o = 2$
- End-point oil relative permeability: $KRO = 0.95$
- End-point oil relative permeability: $KRW = 0.15$

Mixed-wet relative permeability, using Corey correlation

- Corey exponents: $n_w 3,\ n_o = 4$
- End-point oil relative permeability: $KRO = 0.65$
- End-point oil relative permeability: $KRW = 0.55$

Input data for Figure 16

- Viscosity ratio: $M = \mu_w/\mu_o = 0.5$
- Initial water saturation: $S_{wi} = 0.2$
- Initial water saturation: $S_{wi} = 0.15$

Corey relative permeability

- Corey exponents: $n_w = 3,\ n_o = 2$
- End-point oil relative permeability: $KRO = 1.0$
- End-point oil relative permeability: $KRW = 0.23$

LET relative permeability

- End-point oil relative permeability: $KRO = 1.0$

- End-point oil relative permeability: $KRW = 0.20$
- L parameter defining upper part of k_{rw}: $L_w^o = 3.3$
- E parameter defining upper part of k_{rw}: $E_w^o = 2.75$
- T parameter defining upper part of k_{rw}: $T_w^o = 1.25$
- L parameter defining upper part of k_{ro}: $L_o^w = 1.05$
- E parameter defining upper part of k_{ro}: $E_o^w = 35$
- T parameter defining upper part of k_{ro}: $T_o^w = 3.9$

Input data for Figure 17

- Number of grid cells used: $N = 200$
- Time used for saturation plots: $t = (0.1, 0.25, 0.5, 1, 5, 10)$
- Viscosity ratio: $M = \mu_w/\mu_o = 0.5$
- Initial water saturation: $S_{wi} = 0.2$
- Initial water saturation: $S_{wi} = 0.15$

Corey relative permeability

- Corey exponents: $n_w = 3,\ n_o = 2$
- End-point oil relative permeability: $KRO = 1.0$
- End-point oil relative permeability: $KRW = 0.23$

LET relative permeability

- End-point oil relative permeability: $KRO = 1.0$
- End-point oil relative permeability: $KRW = 0.20$
- L parameter defining upper part of k_{rw}: $L_w^o = 3.3$
- E parameter defining upper part of k_{rw}: $E_w^o = 2.75$
- T parameter defining upper part of k_{rw}: $T_w^o = 1.25$
- L parameter defining upper part of k_{ro}: $L_o^w = 1.05$
- E parameter defining upper part of k_{ro}: $E_o^w = 35$
- T parameter defining upper part of k_{ro}: $T_o^w = 3.9$

Input data for Figure 18

- Number of grid cells used: $N = 200$
- Time used for recovery plot: $t = 10$
- Viscosity ratio: $M = \mu_w/\mu_o = 0.5$
- Initial water saturation: $S_{wi} = 0.2$
- Initial water saturation: $S_{wi} = 0.15$

Corey relative permeability

- Corey exponents: $n_w = 3,\ n_o = 2$
- End-point oil relative permeability: $KRO = 1.0$
- End-point oil relative permeability: $KRW = 0.23$

LET relative permeability

- End-point oil relative permeability: $KRO = 1.0$
- End-point oil relative permeability: $KRW = 0.20$
- L parameter defining upper part of k_{rw}: $L_w^o = 3.3$
- E parameter defining upper part of k_{rw}: $E_w^o = 2.75$
- T parameter defining upper part of k_{rw}: $T_w^o = 1.25$
- L parameter defining upper part of k_{ro}: $L_o^w = 1.05$
- E parameter defining upper part of k_{ro}: $E_o^w = 35$
- T parameter defining upper part of k_{ro}: $T_o^w = 3.9$

Appendix B: Input data for gravity expansion

- Number of grid cells used: $N = 500$
- Time used for saturation plots: $t = (0.1, 0.5, 1.0, 5.0)$
- Time used for recovery plot: $t = 5.0$
- Corey exponents: $n_w = 2,\ n_o = 2$
- Water viscosity: $\mu_w = 0.3$ cP $= 0.3 \cdot 10^{-3}$ Pa · s
- Viscosity ratio: $M = \mu_w/\mu_o = 0.5$
- Dip angle: $\alpha = (0°, 1°, 6°, 24°)$
- Dimensionless gravity term: $G = (0.0, 0.46, 2.8, 10.8)$

Constant input parameters in G

- Absolute permeability: $k = 500$ mD $= 500 \cdot 0.987 \cdot 10^{-15}$ m^2
- Density difference: $\Delta\rho = 0.19$ g/cm^3 $= 190$ kg/m^3
- Gravity constant: $g = 9.81$ m/s^2
- Oil viscosity: $\mu_o = 0.6$ cP $= 0.6 \cdot 10^{-3}$ Pa · s
- Total velocity: $u = 0.01$ m/day $= 1.157 \cdot 10^{-7}$ m/s

Appendix C: Input data for capillary pressure expansion

Grid and time input data

- Number of grid cells used: $N = 100$
- Time used for saturation plots: $t = (0.1, 0.5, 1.0, 10.0)$
- Time used for recovery plot: $t = 10.0$

Other parameters

- Water viscosity: $\mu_w = 0.3$ cP $= 0.3 \cdot 10^{-3}$ Pa $\cdot$ s
- Oil viscosity: $\mu_o = 0.6$ cP $= 0.6 \cdot 10^{-3}$ Pa $\cdot$ s
- Viscosity ratio: $M = \mu_w/\mu_o = 0.5$
- Dimensionless constant: $\varepsilon = (0, 1, 100, 10000)$

Relative permeability input data

Water-wet relative permeability, using Corey correlation

- Corey exponents: $n_w = 2,\ n_o = 3$
- End-point oil relative permeability: $KRO = 0.95$
- End-point oil relative permeability: $KRW = 0.15$

Input data for capillary pressure functions

Water-wet capillary pressure , using LET correlation

- Maximum capillary pressure: $P_c^{si} = 1$ bar $= 1 \cdot 10^5$Pa
- L parameter defining upper part: $L^{si} = 0.1$
- E parameter defining upper part : $E^{si} = 27$
- T parameter defining upper part : $T^{si} = 1$
- Maximum capillary pressure: $P_c^{fi} = -0.08$ bar $= -0.6 \cdot 10^5$Pa
- L parameter defining upper part: $L^{fi} = 15$
- E parameter defining upper part : $E^{fi} = 20$
- T parameter defining upper part : $T^{fi} = 1$

Table 1: Some examples of epsilon values

Case	k (mD)	Pc,ref (bar)	μo (cP)	u (m/day)	L (m)	ε
Core scale	50	1	0.300	0.010	0.04	3.55E+03
	50	1	0.300	0.010	100	1.42E+00
Res scale	50	1	0.300	0.010	1000	1.42E-01
Data from [1]	500	1*	0.300	0.010	0.04	3.55E+04
	500	1	0.300	0.010	100	1.42E+01
Res scale	500	1	0.300	0.010	1000	1.42E+00
Core scale	1000	1	0.300	0.010	0.04	7.11E+04
	1000	1	0.300	0.010	100	2.84E+01
	1000	1	0.300	0.010	1000	2.84E+00
Core scale	500	1	0.600	0.010	0.04	1.78E+04
	500	1	0.600	0.010	100	7.11E+00
Res scale	500	1	0.600	0.010	1000	7.11E-01
Core scale	500	1	0.300	0.010	0.04	3.55E+04
	500	1	0.300	0.010	100	1.42E+01
Res scale	500	1	0.300	0.010	1000	1.42E+00
Core scale	500	1	0.100	0.010	0.04	1.07E+05
	500	1	0.100	0.010	100	4.26E+01
	500	1	0.100	0.010	1000	4.26E+00
Core scale	500	1	0.300	0.100	0.04	3.55E+03
	500	1	0.300	0.100	100	1.42E+00
Res scale	500	1	0.300	0.100	1000	1.42E-01
Core scale	500	1	0.300	0.050	0.04	7.11E+03
	500	1	0.300	0.050	100	2.84E+00
Res scale	500	1	0.300	0.050	1000	2.84E-01
Core scale	500	1	0.300	0.010	0.04	3.55E+04
	500	1	0.300	0.010	100	1.42E+01
Res scale	500	1	0.300	0.010	1000	1.42E+00

*data not taken from [1], this data is assumed.

Appendix D: Input data for the low salinity model

Input data for relative permeability functions

High salinity conditions: these values are based on oil-wet conditions.

$$KRW^{ow} = 0.3, \qquad KRO^{ow} = 0.75$$

$$S_{wi}^{ow} = 0.15, \qquad S_{or}^{ow} = 0.3$$

$$no^{ow} = 3, \qquad nw^{ow} = 2$$

Low salinity conditions: these values are based on water-wet conditions.

$$KRW^{ww} = 0.4, \qquad KRO^{ww} = 0.9,$$

$$S_{wi}^{ww} = 0.15, \qquad S_{or}^{ww} = 0.15$$

$$no^{ww} = 3, \qquad nw^{ww} = 2$$

Activity coefficients used to define parameters in (5.1), (5.2) and (5.3)

$$a_{ca}^0 = 5,\ a_{na}^0 = 4,\ \ a_{cl}^0 = 3.5,\ \ a_{mg}^0 = 5.5,\ \ a_{so}^0 = 5$$

$$b_{ca}^0 = 0.165,\ b_{na}^0 = 0.075,\ b_{cl}^0 = 0.015,\ b_{mg}^0 = 0.2,\ \ b_{so}^0 = -0.04$$

$$A(T = 80) = 0.5706,\ B(T = 80) = 0.3381$$

Core properties

- Length: $L = 0.04$ m
- Porosity: $\varphi = 0.274$
- Mas of clay: $M_c = 0.088$ kg/litre core
- Absolute permeability: $k = 500$ mD $= 500 \cdot 0.987 \cdot 10^{-15}$ m^2

Oil and brine properties

- Oil viscosity: $\mu_o = 0.6$ cP $= 0.6 \cdot 10^{-3}$ Pa $\cdot$ s
- Brine viscosity: $\mu_w = 0.3$ cP $= 0.3 \cdot 10^{-3}$ Pa $\cdot$ s

Properties connected to MIE

- Cation exchange capacity: $CEC = 0.013$ eq/kg clay
- Selectivity factor: $K_{cana}^{HS} = 5.1,\ K_{cana}^{LS} = 1.7$
- Selectivity factor: $K_{mgna}^{HS} = 4.8,\ K_{mgna}^{LS} = 1.6$
- Corresponding brine salinity: $B_s^{HS} = 4.5,\ B_s^{LS} = 10^{-8}$
- r constant: $r = 400$

Other properties

- Total velocity: $v_T = 0.01$ m/day $= 1.1574 \cdot 10^{-7}$ m/s
- Reference diffusion coefficient: $D_{m,ref} = Lv_T = 4.6296 \cdot 10^{-9}\ \mathrm{m}^2/\mathrm{s} \approx 5 \cdot 10^{-9}\ \mathrm{m}^2/\mathrm{s}$
- Reference viscosity: $\mu_{ref} = 10^{-3}$ Pa · s

Oil recovery

$$N_p = \frac{\int_0^1 [S(x,t) - S_{wi}(x)]dx}{\int_0^1 [1 - S_{wi}(x)]dx}$$

Formation water and brine compositions

Table 2: Composition of formation water (FW) and different brine compositions (LSW, LSW1, LSW2 and LSW3)

Ions	FW [mol/l]	LSW [mol/l]	LSW1 [mol/l]	LSW2 [mol/l]	LSW3 [mol/l]
Na^+	1.3262	0.013262	0.13262	0.13262	0. 13262
Cl^-	1.6569	0.016570	0.17050	0.13907	0.13266
Ca^{2+}	0.1479	0.001479	0.00148	0.00148	0.00001
Mg^{2+}	0.0175	0.000175	0.01746	0.00175	0.00001
SO_4^{2-}	0.0000	0.000000	0.00000	0.00000	0.00000
I_o	1.8224	0.018224	0.18944	0.17373	0.13616